

# Directional Codes: a new family of quantum LDPC codes on hexagonal- and square-grid connectivity hardware

György P. Gehér<sup>1,2</sup>, David Byfield<sup>1,2</sup>, and Archibald Ruban<sup>1</sup>

<sup>1</sup>Riverlane, St. Andrew's House, 59 St. Andrew's Street, Cambridge CB2 3BZ, United Kingdom

<sup>2</sup>These two authors are joint first authors

Utility-scale quantum computing requires quantum error correction (QEC) to protect quantum information against noise. Currently, superconducting hardware is a promising candidate for achieving fault tolerance due to its fast gate times and feasible scalability. However, it is often restricted to two-dimensional nearest-neighbour connectivity, which is thought to be incapable of accommodating high-rate quantum low-density parity-check (qLDPC) codes that promise to greatly reduce the number of physical qubits needed to encode logical qubits. In this paper we construct a new family of qLDPC codes, which we call “Directional Codes”, that outperforms the rotated planar code (RPC) while naturally meeting the connectivity requirements of the widely adopted square-grid, and some even the sparser hexagonal-grid. The key idea is to utilise the iSWAP gate – a natural native gate for superconducting qubits – to construct circuits that measure the stabilisers of these qLDPC codes without the need for any long-range connections or an increased degree of connectivity. We numerically evaluate the performance of directional codes, encoding four, six and twelve logical qubits, using a common superconducting-inspired circuit-level Pauli noise model. We also compare them to the RPC and to the bivariate bicycle (BB) codes, currently the two most popular quantum LDPC code families. As a concrete example, directional codes outperform the RPC by achieving approximately the same logical error probability at physical error rate  $p = 10^{-3}$  using only 18.75 – 45% of the physical qubits at distance up to 10. Our discovery represents a breakthrough in QEC code design that suggests complex long-range, high-connectivity hardware may not be necessary for low-overhead fault-tolerant quantum computation.

## 1 Introduction

Quantum computers have the potential to solve problems which would be intractable on a classical computer [1–4]. However, qubits are inherently very noisy (much noisier than classical bits), and therefore it is largely believed that quantum error correction (QEC) is an essential part of achieving useful quantum computation [5–7]. In QEC we use a number of physical qubits to encode a smaller number of logical qubits – referred to as

György P. Gehér: [george.geher@riverlane.com](mailto:george.geher@riverlane.com), [gehergyuri@gmail.com](mailto:gehergyuri@gmail.com)

David Byfield: [david.byfield@riverlane.com](mailto:david.byfield@riverlane.com), [david.s.byfield@gmail.com](mailto:david.s.byfield@gmail.com)

a QEC code – by repeatedly measuring a set of Pauli-product operators (or stabilisers) on the physical qubits. If we gain enough information about the errors on the physical qubits, we can then protect the logical qubits and ultimately implement algorithms with them [8–10].

Superconducting qubits are a strong contender for useful quantum computing due to their typically very fast gates [11–16] and potential scalability [17, 18]. However, they usually come with the draw-back of restricted connectivity, meaning a two-qubit gate can be executed only between a limited number of pairs of qubits. Typically, each qubit is connected to at most four others, as is the case for e.g. the “square-grid” or “hexagonal-grid” connectivity (Figure 1), which have so far been the most commonly realised connectivities for quantum hardware demonstrations [11–15, 19]. This constraint poses a challenge for QEC code design, since on most hardware a syndrome extraction circuit [20, 21] is needed to measure a Pauli-product operator on multiple qubits through the measurement of an ancilla qubit. This typically requires that the ancilla qubit and the qubits that support the operator are connected, thereby restricting the possible QEC codes implementable on such hardware [22].



Figure 1: Hardware layouts with square- and hexagonal-grid connectivity. All the codes constructed in this paper can be executed on the square-grid (a), and some of them even on the hexagonal-grid (b). The qubits are coloured with red and black, corresponding to ancilla and data qubits.

Quantum low-density parity-check (qLDPC) codes [22–24] are an exciting family of QEC codes that can provide high encoding rates [25, 26]. However, they often require long-range connections (i.e. connections not part of the square-grid, see Figure 1a) and an increased degree of connectivity (i.e. each qubit needs to be connected to more than four qubits), which have so far proven challenging to implement [18, 27]. The rotated planar code (RPC) is a popular example of a qLDPC code with a relatively poor encoding rate [20], but with the advantage that it is easily implementable under the natural square-grid connectivity.

To date, we do not know of any qLDPC codes with a notably higher encoding rate than the RPC that do not require connectivity beyond the square-grid. Probably the most popular example of a qLDPC code family with higher encoding rate than the RPC is that of the bivariate bicycle (BB) codes [18, 28]. However, they require the addition of two long-range connections per qubit, increasing the degree of connectivity from four to six, see [28, Figure 1] and also [29, 30].

In this paper we demonstrate that it is possible to construct qLDPC codes with higher encoding rate than the RPC, while being implementable under square-grid connectivity (Figure 1a), and even some of them under the sparser hexagonal-grid connectivity (Figure 1b). We call this family “directional codes”, and they arise very naturally if we have access to iSWAP as a native entangling gate on the hardware. The key idea in the construction of our directional codes is that iSWAP exchanges the state between the two qubits it acts on. This is in general considered to be more of a hindrance, as it makes circuit construction more complex [15, 31]. However, as we show here, we may exploit this trait of the iSWAP gate to our advantage.

The controlled-phase (CZ) gates (and their equivalents) are currently a more popular choice of native gate, partly because it is well-known how to build syndrome extraction circuits with them. However, on superconducting hardware, the iSWAP may be a more advantageous choice as the native two-qubit gate, and we point out that such devices have been built already, see e.g. [15, 32–34]. For example, a recent hardware demonstration [15] emphasises the potential of the iSWAP gate as the future standard entangling gate for superconducting hardware through its strong leakage suppression and low error rates. This is especially exciting when considering the progress seen over the past ten years for the CZ gate [15, 35–40], which we may also reasonably expect from the iSWAP gate in the coming years. Furthermore, [15] highlights the importance of lowering connectivity requirements as much as possible, showing a  $\approx 15\%$  improvement in the error suppression factor  $\Lambda$  when operating only the couplers needed for hexagonal-grid connectivity, i.e. decreasing the connectivity per qubit by one. This makes a strong case for further exploration of the ideas presented in this paper as an alternative to the costly and complex development of long-range, high-connectivity hardware, like that proposed in [18].

The structure of our paper is as follows. In the next section we explain our method to construct circuits that measure a set of Pauli-product operators that constitute the stabilisers of this novel family of Calderbank–Shor–Steane (CSS) codes. We first explain the circuit construction on an infinite plane, and then wrap around a generalised torus to obtain a CSS code. We also collect all possible families that have stabilisers of weight at least four and at most seven, and categorise them according to whether they can be implemented on hexagonal-grid or only on square-grid. In Section 3, we present simulation results for three families of directional codes, one with weight-5 stabilisers encoding four logical qubits, the second with weight-6 stabilisers encoding six logical qubits, and the last with weight-7 stabilisers encoding twelve logical qubits. Our numerical results indicate that directional codes outperform the RPC under circuit-level Pauli noise. For instance, at physical error rate  $p = 10^{-3}$  we achieve approximately the same logical error probability using only 18.75 – 45% of the physical qubits. In Section 4 we conclude the paper with some discussion on our results and potential future work. This includes adding boundaries to enable planar rather than toric hardware. The Appendix contains additional insight into the structure of directional codes and some further numerical results.

## 2 Construction of directional codes

Our stabiliser codes are constructed by defining their associated syndrome extraction circuits that by design meet the square-grid connectivity constraint, see Figure 1a. We will also see that some of these codes do not require the full connectivity of the square-grid architecture, and thus can be executed on the sparser hexagonal-grid. We achieve this by using iSWAP as the native two-qubit gate, instead of the popular choices like CZ.

We recall that the CXSWAP gate on control qubit  $Q_0$  and target qubit  $Q_1$  is defined by

$$\text{CXSWAP}(Q_0, Q_1)|\psi\rangle = \text{SWAP}(Q_0, Q_1)\text{CX}(Q_0, Q_1)|\psi\rangle, \quad (1)$$

i.e. it is equivalent to applying a CX gate followed by a SWAP gate. CZSWAP is defined similarly, and for the sake of brevity we will often refer to these two gates as CPSWAP gates. It is well-known that the CPSWAP gates are KAK-equivalent to the iSWAP gate [31, Section A.5], more precisely we can find one-qubit unitary Clifford gates  $A_0, A_1, B_0, B_1$  such that

$$\text{CPSWAP}(Q_0, Q_1) = A_0 \otimes A_1 \cdot \text{iSWAP}(Q_0, Q_1) \cdot B_0 \otimes B_1. \quad (2)$$

Therefore, if we construct a syndrome extraction circuit in terms of CPSWAP gates, obtaining one that uses iSWAPs instead is a matter of compilation. We prefer to use CPSWAP gates in our construction instead of iSWAP gates because the swapping action of the gate is clearly separated from the action of the controlled-Pauli gate. In fact, we can think of a layer of CPSWAP gates as being a layer of controlled-Pauli gates up to permutation of the quantum states on the physical qubits – we leverage this heavily in our constructions.

After showing a motivating example in Section 2.1, we explain our code construction method in three steps, detailed in Sections 2.2 to 2.4. First, we consider the infinite planar square-grid lattice  $\mathbb{Z}^2$  with square-grid connectivity, and describe how we can measure a set of  $X$ -stabilisers whose data qubits are not all connected to a single (ancilla) qubit. Second, we consider what happens if we naively apply this circuit-construction method to arbitrary stabiliser types. In order to obtain a valid circuit that measures these stabilisers simultaneously and independently, we need to avoid entangling the ancilla qubits, see e.g. [41]. We prove a theorem that characterises when this is the case. Finally, in order to get a CSS code that encodes logical qubits, we need to make the lattice finite. We achieve this by wrapping  $\mathbb{Z}^2$  around a generalised torus. We also collect all the symmetric CSS code types that we can obtain in such a way with stabiliser weights 4, 5, 6 and 7, though the construction is valid for arbitrarily high weight. The weight-4 case, an example of which is shown in Section 2.1, provides a linear transformed version of the toric code. However, the higher weight versions provide novel CSS codes that have better encoding rates than the RPC, while still being executable under low connectivity constraints. It is important to note that our construction specifies the syndrome extraction circuits for our codes implicitly.

## 2.1 Motivating example

Consider a  $6 \times 6$  square with toric boundary conditions, on which we place qubits in a square-grid fashion, with the bottom-left-most qubit being a data qubit. As shown in Figure 2, we apply a sequence of four CPSWAP layers, along with the necessary resets before and measurements after on the ancilla qubits, to perform syndrome extraction. The first layer, with vertically oriented gates, has the effect of moving all the data qubits down and the ancillas up. The next two layers, with horizontal gates, each move all the data qubits left and all the ancillas right. We then perform a final vertical layer, again moving the data qubits down and ancillas up.

It is straightforward to see that the stabilisers measured here are closely related to those of the toric code, but with a different shape. In fact, we can think of this example as a linearly transformed version of a distance-3 toric code. In the next few subsections we will formalise this process and describe how we may generalise to higher-weight stabiliser measurements, allowing novel CSS codes to be constructed.

## 2.2 Measuring $X$ -stabilisers on an infinite planar square-grid

Recall that the following circuit measures an  $X$ -stabiliser on data qubits  $\{Q_1, Q_2, \dots, Q_w\}$  by using an ancilla qubit  $A$  (see e.g. [2] or [41, Section 2]): initialise qubit  $A$  in the  $|+\rangle$  state, apply the  $CX(A, Q_1), \dots, CX(A, Q_w)$  gates in this order, and finally measure qubit  $A$  in the  $X$  basis. This measurement outcome on qubit  $A$  corresponds to the  $\prod_{j=1}^w X_{Q_j}$  stabiliser measurement. Denote the circuit defined this way by  $\mathcal{M}(X; A; Q_1, Q_2, \dots, Q_w)$ , which is often called a syndrome extraction circuit. Note that the ordering of the data

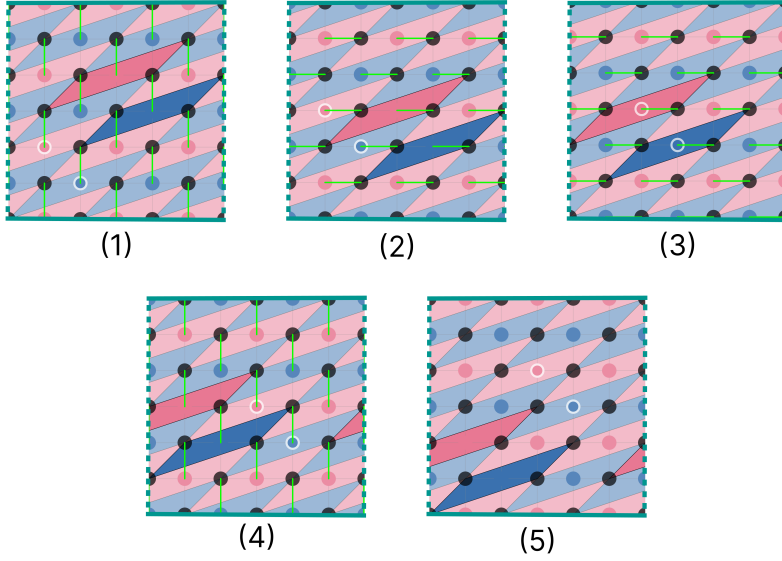


Figure 2: A sequence of layers of CPSWAP gates which measure the stabilisers of a distance-3 toric code on a  $6 \times 6$  torus, which is linearly transformed. The ancilla qubit resets and measurements take place before and after the layers shown, respectively. Each blue (red) parallelogram represents a weight-4  $Z$ - ( $X$ )-stabiliser supported on the four data qubits at its vertices. Data qubits are shown as black dots, and the ancilla qubit corresponding to each  $Z$ - ( $X$ )-stabiliser is shown as a blue (red) dot. Each green line is a CPSWAP between the two qubits it touches, with the ancilla (data) qubit always being the control (target) qubit. The CPSWAP is a CZSWAP (CXSWAP) if the ancilla qubit corresponds to a  $Z$ - ( $X$ )-stabiliser. An  $X$ - and a  $Z$ -stabiliser have been highlighted (and their respective ancilla qubit circled in white) to illustrate the movement of the stabilisers and data qubits relative to the ancilla qubits, as caused by the action of the SWAP-part of each CPSWAP layer. Panel (1)-(4) show the four CPSWAP layers, and panel (5) shows the final configuration.

qubits in this circuit fixes the schedule of the stabiliser, i.e. the order in which entangling gates are applied.

Assume we have a collection of such syndrome extraction circuits that each measure an  $X$ -stabiliser on some data qubits. Suppose further that these circuits use ancilla qubits that are different from each other and also from all data qubits. It is well-known that executing these circuits simultaneously gives a syndrome extraction circuit that measures all the  $X$ -stabilisers simultaneously and independently, provided that no qubit appears in the same layer twice. A crucial assumption here is that all the stabilisers are of the same type,  $X$  (we will consider the more general case in the next subsection).

Next, consider the infinite square-grid lattice  $\mathbb{Z}^2$  on which we lay out data and ancilla qubits in a checkerboard pattern as depicted in Figure 1a. More precisely, define  $\mathbb{Z}_{data}^2 := \{(x, y) \in \mathbb{Z}^2 : x \equiv y \pmod{2}\}$  and  $\mathbb{Z}_{anc}^2 := \mathbb{Z}^2 \setminus \mathbb{Z}_{data}^2$ . We assume that initially we place data qubits on the sublattice  $\mathbb{Z}_{data}^2$  and ancilla qubits on the sublattice  $\mathbb{Z}_{anc}^2$ . Note that any two qubits that are part of the same sublattice are not connected. Each ancilla qubit is connected to four data qubits positioned in the north:  $\vec{n} := (0, 1)$ , east:  $\vec{e} := (1, 0)$ , south:  $\vec{s} := (0, -1)$  and west:  $\vec{w} := (-1, 0)$  directions.

Let us pick one of these directions, say north, and consider the following circuit layer of CXSWAP gates: for each ancilla qubit, apply a CXSWAP between it as control and the data qubit north of it as target, see Figure 3a. Due to the SWAP part of the gates, we may think of each qubit as being interchanged with its pair as an effect of this layer. In this way, the sublattice of ancilla qubits moved north by one unit, while the sublattice of data

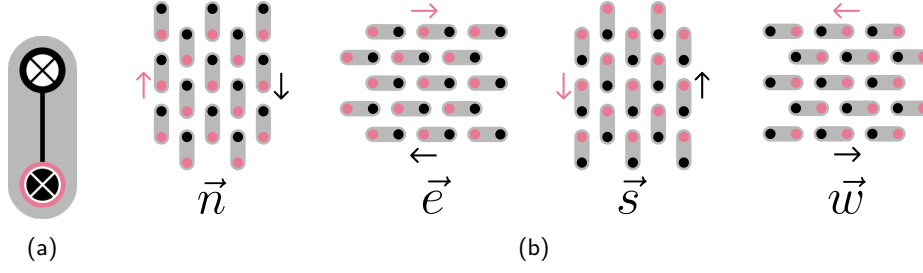


Figure 3: We demonstrate the four types of CPSWAP layers used in the syndrome extraction of directional codes, each corresponding to a direction. (a) A zoomed-in view of the data-ancilla qubit pairs in (b), with overlaid CXSWAP gate. The bottom qubit is the ancilla qubit where the control of the gate is, and the top qubit is the data qubit where the target of the gate is. (b) The four types of CPSWAP layers forming the building blocks of the syndrome extraction circuit construction corresponding to  $\vec{n}$  (north),  $\vec{e}$  (east),  $\vec{s}$  (south), and  $\vec{w}$  (west) directions, respectively. Data and ancilla qubits are shown as black and red nodes, respectively. Red arrows indicate the direction in which the ancilla qubits uniformly move by one unit due to the action of the layer. The data qubits uniformly move in the opposite direction also by one unit, indicated by black arrows. Each grey-highlighted pair of qubits are involved in a CPSWAP gate in that layer. The CPSWAP's control is always the ancilla and target always the data qubit, as depicted in a) for the CXSWAP case.

qubits moved in the opposite direction, south, by one unit - see Figure 3b. Consequently, each ancilla qubit is now connected to three data qubits it was not connected to before, while it remains connected to the data qubit that has just been involved in the same CXSWAP gate. Therefore, even though the relative location of ancilla/data qubits did not change, the connectivity structure between the two sublattices changed considerably. This is a crucial observation that is the core idea for our code construction.

Consider an arbitrary sequence of directions:  $\vec{d}_1, \vec{d}_2, \dots, \vec{d}_w$ , where  $\vec{d}_j \in \{\vec{n}, \vec{e}, \vec{s}, \vec{w}\}$ . We describe how the ancilla qubits move in the frame of reference of the data qubit sublattice if we were to execute the series of CXSWAP layers according to  $\vec{d}_1, \vec{d}_2, \dots, \vec{d}_w$ . Since in each layer the two sublattices move in opposite directions on the hardware, in the frame of reference of the data qubit sublattice the ancilla qubits always move twice the length. Thus in the data qubits' frame of reference, if the ancilla qubit started at position  $A_0$  and after the first  $j$  layers it got shifted to  $A_j$ , then the vector pointing from the former to the latter position is  $\overrightarrow{A_0 A_j} = 2 \sum_{\ell=1}^j \vec{d}_\ell$ . Therefore, given that the data qubits just moved in the opposite direction, the vector that points from the original position of the ancilla qubit  $A_0$  to the current position of the data qubit  $Q_j$  it just interacted with is

$$\overrightarrow{A_0 Q_j} = \overrightarrow{A_0 A_j} - \vec{d}_j = 2 \sum_{\ell=1}^{j-1} \vec{d}_\ell + \vec{d}_j, \quad (3)$$

see Figure 4.

We define the set of *delta vectors* associated with the sequence of directions  $\vec{d}_1, \vec{d}_2, \dots, \vec{d}_w$  as the set of vectors that point from an earlier scheduled data qubit  $Q_i$  to a later scheduled one  $Q_j$ . More precisely, using (3) this set can be written as

$$\Delta = \Delta(\vec{d}_1, \vec{d}_2, \dots, \vec{d}_w) := \left\{ \overrightarrow{Q_i Q_j} = \vec{d}_i + 2 \sum_{\ell=i+1}^{j-1} \vec{d}_\ell + \vec{d}_j : 1 \leq i < j \leq w \right\}. \quad (4)$$

Notice that the zero vector is not a delta vector if and only if a given ancilla qubit and any of the data qubits interact only once. Throughout the paper we always assume  $\vec{0} \notin \Delta$ .



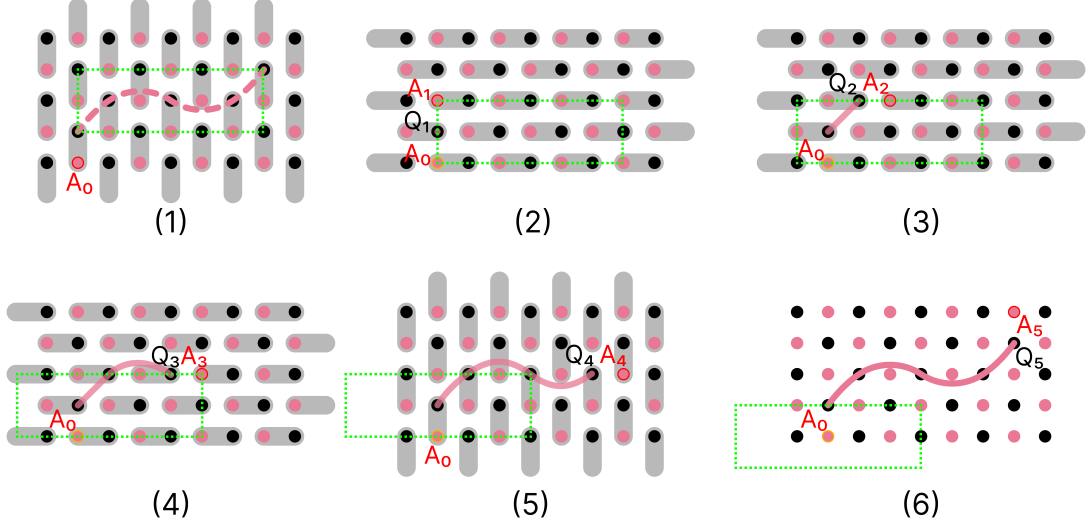


Figure 4: Illustration of CXSWAP layers executed according to the sequence of directions  $\vec{n}, \vec{e}, \vec{e}, \vec{e}, \vec{n}$ , shown in the data qubits' frame of reference. These layers appear in the syndrome extraction circuit of  $NE^3N$ -stabilisers, all of  $X$ -type here, although note that varying stabiliser types is also possible with  $NE^3N$ -stabilisers, see Figures 6 and 8 and Table 1. (1)-(6) show how the ancilla qubit of a given stabiliser moves ( $A_0, A_1, \dots, A_5$ ) under the action of each layer to reach all its data qubits ( $Q_1, \dots, Q_5$ ). Data qubits are shown as black nodes, and ancilla qubits as red nodes. Grey highlighted pairs of qubits are involved in a CXSWAP together in that layer, as in Figure 3a. The CXSWAP's control is always the ancilla and target always the data qubit. The red dashed snake-like shape shown in (1) is an  $NE^3N$ -stabiliser whose Pauli terms are collected by the ancilla qubit circled in red. The shape fills up as each of its data qubits are covered by a CXSWAP gate with the ancilla qubit as control. Since each panel is shown in the data qubits' frame of reference, the stabiliser appears static throughout, even though on the hardware it is constantly sliding. This is illustrated by the green dashed box, which represents a fixed section of hardware across which the qubits move. As shown, the stabiliser slides out of that region, as we apply the CXSWAP layers.

Furthermore, the delta vectors are useful to capture scheduling conflicts (see conditions (a)–(c) in Section 2.3) and we will use it heavily in the proof of Theorem 1.

Now, consider the circuit where we start by initialising all ancilla qubits in the  $|+\rangle$  state, then execute a series of CXSWAP gates according to the sequence of directions  $\vec{d}_1, \vec{d}_2, \dots, \vec{d}_w$ , and finally measure all ancilla qubits (at their final location) in the  $X$  basis. Then, based on the above observations, we measured an infinite set of  $X$ -stabilisers simultaneously and independently. More precisely, all stabilisers have the same shape, i.e. for each ancilla qubit that in the beginning is placed at  $A_0$  in the frame of reference of the data qubit sublattice, the stabiliser which was measured by this ancilla is  $\prod_{j=1}^w X_{Q_j}$ , and throughout the circuit the ancilla itself moved to position  $A_w$  where it was measured. We call stabilisers obtained in such a way a  $D_1 D_2 \dots D_w$ -stabiliser, where  $D_j$  stands for the capitalised version of  $\vec{d}_j$  without the arrow. Later on, when we define a CSS code with  $D_1 D_2 \dots D_w$ -stabilisers, we will refer to it as a  $D_1 D_2 \dots D_w$ -code, for the sake of simplicity. As an example, a CSS code defined by the direction sequence  $\vec{n}, \vec{e}, \vec{e}, \vec{n}$  is an example of an  $NEEN$ -code, or equivalently an  $NE^2N$ -code, as in Section 2.1. Similarly, the  $\vec{n}, \vec{e}, \vec{e}, \vec{e}, \vec{n}$  direction sequence gives  $NE^3N$ -stabilisers, see Figure 4.

If we wish to measure these stabilisers for a second time, we could continue by executing a circuit according to the reversed direction sequence  $\vec{d}_w, \vec{d}_{w-1}, \dots, \vec{d}_1$ . If we wish to measure them more times, we could apply these two circuits repeatedly one after the other. In this way the stabilisers on the hardware move back and forth. Note that in

principle we could use the same direction sequence all the time, but then the stabilisers would move in the same direction on the hardware, and as a result eventually would leave any finite area of  $\mathbb{Z}^2$ .

### 2.3 Measuring stabilisers of varying Pauli types on an infinite planar square-grid

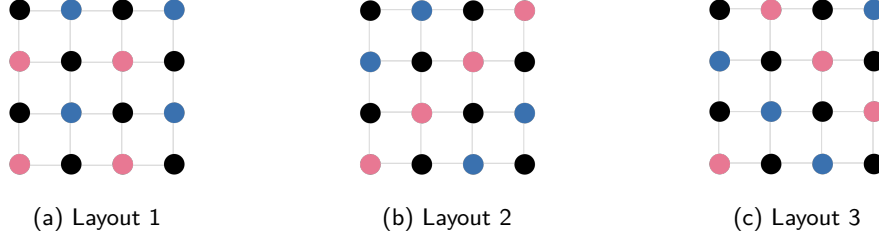


Figure 5: The three typical layouts  $\alpha$  for allocating stabilisers for a directional code, although other valid layouts do exist. Data/ $X$ -ancilla/ $Z$ -ancilla qubits are shown as black/red/blue dots.

The goal of this subsection is to construct circuits on  $\mathbb{Z}^2$  that measure an infinite set of  $X$ - and  $Z$ -stabilisers simultaneously and independently using CPSWAP gates. Recall that in the previous subsection it was a crucial assumption that all stabilisers had the same Pauli type. However, when we combine circuits that separately measure stabilisers of different Pauli types, we have to be more careful not to entangle the ancilla qubits.

First, consider circuits that use controlled-Pauli gates. Denote by  $\mathcal{M}(Z; A; Q_1, Q_2, \dots, Q_w)$  the circuit we obtain from  $\mathcal{M}(X; A; Q_1, Q_2, \dots, Q_w)$  (defined at the beginning of Section 2.2) by replacing all CX gates by CZ gates. It is well-known that  $\mathcal{M}(Z; A; Q_1, Q_2, \dots, Q_w)$  measures the stabiliser  $\prod_{j=1}^w Z_{Q_j}$ . Consider now the two circuits  $\mathcal{M}(X; A; Q_1, Q_2, \dots, Q_w)$  and  $\mathcal{M}(Z; A'; Q'_1, Q'_2, \dots, Q'_w)$ , where  $A$  and  $A'$  are different and disjoint from  $\{Q_1, \dots, Q_w\} \cup \{Q'_1, \dots, Q'_w\}$ . Recall that when we combine these circuits so that they happen simultaneously, we get a circuit that measures  $\prod_{j=1}^w X_{Q_j}$  and  $\prod_{j=1}^w Z_{Q'_j}$  simultaneously and independently if and only if the following three conditions are satisfied:

- (a)  $Q_j \neq Q'_j$  for all  $j = 1, \dots, w$ ;
- (b) the set  $\{(i, j): Q_i = Q'_j, i < j\}$  has evenly many elements;
- (c) the set  $\{(i, j): Q_i = Q'_j, i > j\}$  has evenly many elements;

see e.g. [41, Section 2]. Condition (b)/(c) means that among the shared data qubits between the two stabilisers, evenly many are scheduled earlier/later in the circuit  $\mathcal{M}(X; A; Q_1, Q_2, \dots, Q_w)$  than in  $\mathcal{M}(Z; A'; Q'_1, Q'_2, \dots, Q'_w)$ . Furthermore, conditions (a)–(c) ensure that when we combine the circuits the ancilla qubits do not get entangled, and that the stabilisers  $\prod_{j=1}^w X_{Q_j}$  and  $\prod_{j=1}^w Z_{Q'_j}$  commute. We also point out that in case the Pauli type of the two stabilisers were the same, then only condition (a) needs to be satisfied, as was the case in Section 2.2.

Next, we call a mapping  $\alpha: \mathbb{Z}_{anc}^2 \rightarrow \{X, Z\}$  a “layout”. In the rest of the paper a layout will determine the location of the ancillas for each stabiliser type. For instance, the layout where we have alternating rows of  $X$ - and  $Z$ -stabilisers we call “Layout 1” (Figure 5a), the layout where we have alternating diagonals travelling north-east we call “Layout 2” (Figure 5b), and the one where we have alternating diagonals travelling north-west we call “Layout 3” (Figure 5c). These three layouts were the most common during our investigation.



Now, we discuss circuits that use CPSWAP gates. Previously, we denoted by  $A_j$  the position of the ancilla qubit of a stabiliser after the  $j$ th CPSWAP layer in the data qubits' frame of reference. We introduce the notation  $A(j)$  for the position of the same qubit in the hardware's frame of reference. Consider a direction sequence  $\vec{d}_1, \vec{d}_2, \dots, \vec{d}_w$ , and a layout  $\alpha: \mathbb{Z}_{anc}^2 \rightarrow \{X, Z\}$ . We define the circuit  $\mathcal{C}(\alpha; \vec{d}_1, \vec{d}_2, \dots, \vec{d}_w)$  in the following way.

- (0) Reset all ancilla qubits  $A \in \mathbb{Z}_{anc}^2$  in the  $|+\rangle$  state.
- ( $j$ ) ( $1 \leq j \leq w$ ) For each initial ancilla qubit position  $A$  track where it is now due to the previous steps:  $A(j-1) = A + \sum_{\ell=1}^{j-1} \vec{d}_\ell$ . At each of these apply the CXSWAP( $A(j-1), A(j-1) + \vec{d}_j$ ) gate if  $\alpha(A) = X$ , otherwise the CZSWAP( $A(j-1), A(j-1) + \vec{d}_j$ ) gate. Due to this layer, the ancilla qubit is now at  $A(j) = A + \sum_{\ell=1}^j \vec{d}_\ell$ .
- ( $w+1$ ) Measure all ancilla qubits at their current locations  $A(w)$  in  $X$  basis.

Note that the circuit from the previous subsection is  $\mathcal{C}(\alpha_X; \vec{d}_1, \vec{d}_2, \dots, \vec{d}_w)$  where  $\alpha_X$  is the mapping that has value  $X$  everywhere. We saw that this circuit measures simultaneously and independently  $D_1 D_2 \dots D_w$ -stabilisers of  $X$ -type associated with all ancilla qubits.

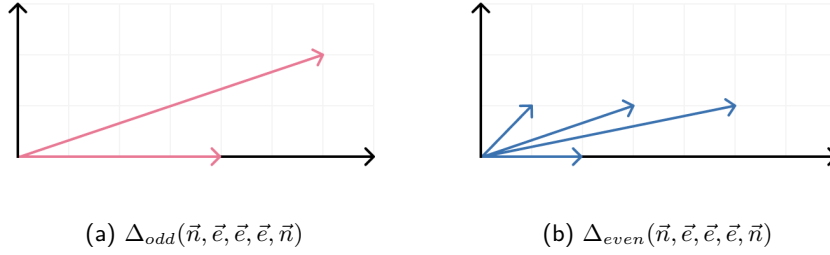


Figure 6: Delta vectors of an  $NE^3N$ -stabiliser. (a) The vectors from  $\Delta_{odd}(\vec{n}, \vec{e}, \vec{e}, \vec{e}, \vec{n})$  each shown in red. (b) The vectors from  $\Delta_{even}(\vec{n}, \vec{e}, \vec{e}, \vec{e}, \vec{n})$  each shown in blue.

In Theorem 1 below our goal is to establish a set of “if and only if” conditions that the circuit  $\mathcal{C}(\alpha; \vec{d}_1, \vec{d}_2, \dots, \vec{d}_w)$  needs to meet so that it measures the  $D_1 D_2 \dots D_w$ -stabiliser of  $\alpha(A)$ -type, for all  $A \in \mathbb{Z}_{anc}^2$ , simultaneously and independently. Since each CPSWAP layer moves the data qubit sublattice uniformly in one direction (see Figure 3b), we can use conditions (a)–(c) above in the data qubits' frame of reference for the CPSWAP case to validate circuits of the form  $\mathcal{C}(\alpha; \vec{d}_1, \vec{d}_2, \dots, \vec{d}_w)$ . The following subsets of delta vectors (4) are useful to capture (b)–(c), and we will use them in the proof:

$$\Delta_{odd} = \Delta_{odd}(\vec{d}_1, \vec{d}_2, \dots, \vec{d}_w) := \left\{ \vec{v} \in \Delta : \vec{v} = \overrightarrow{Q_i Q_j} \text{ for odd many } (i, j), 1 \leq i < j \leq w \right\}, \quad (5)$$

$$\Delta_{even} = \Delta_{even}(\vec{d}_1, \vec{d}_2, \dots, \vec{d}_w) := \Delta \setminus \Delta_{odd}. \quad (6)$$

In other words,  $\Delta_{odd}$  is the set of delta vectors that appear odd many times, and  $\Delta_{even}$  is the set of those that appear evenly many (but at least two) times. These sets are illustrated for  $NE^3N$ -stabilisers in Figure 6.

For a given set of vectors  $S \subset \mathbb{Z}^2$ , denote by  $\text{SPAN}_{\mathbb{Z}}(S)$  the set of all vectors that are linear combinations of vectors from  $S$  with integer coefficients. Now, we are able to state and prove our theorem.

**Theorem 1.** Consider a sequence of directions  $\vec{d}_1, \vec{d}_2, \dots, \vec{d}_w$  ( $\vec{d}_j \in \{\vec{n}, \vec{e}, \vec{s}, \vec{w}\}$ ,  $w \in \mathbb{Z}, w > 0$ ) and a layout  $\alpha: \mathbb{Z}_{anc}^2 \rightarrow \{X, Z\}$ . Assume  $\vec{0} \notin \Delta$ . Define the sub-lattice

$\mathcal{L} := \text{SPAN}_{\mathbb{Z}}(\Delta_{\text{odd}})$ . Then the circuit  $\mathcal{C}(\alpha; \vec{d}_1, \vec{d}_2, \dots, \vec{d}_w)$  measures all the  $D_1 D_2 \dots D_w$ -stabilisers simultaneously and independently according to the layout  $\alpha$  if and only if

$$\alpha(A) = \alpha(A') \text{ holds for all } A, A' \in \mathbb{Z}_{\text{anc}}^2, \overrightarrow{AA'} \in \mathcal{L}. \quad (7)$$

Before we prove our theorem, we explain its meaning through some special cases. According to the theorem the only restriction on the layout  $\alpha$  is forced via the sublattice  $\mathcal{L}$ , but otherwise we are free to choose the type of the ancilla qubits. Consider the case of the  $NE^2N$ -stabilisers. Since we have  $\Delta(\vec{n}, \vec{e}, \vec{e}, \vec{n})_{\text{odd}} = \{2\vec{e}, 4\vec{e} + 2\vec{n}\}$ , we have  $\mathcal{L} = \{2x\vec{n}, 2y\vec{e} : x, y \in \mathbb{Z}\}$ . Therefore, a valid layout  $\alpha$  for the  $NE^2N$  case needs to be constant on both sublattices  $\mathcal{L}$  and  $\mathcal{L} + \vec{e} + \vec{n}$ . In particular, we may only get a quantum CSS code (after wrapping around a torus, see Section 2.4) if  $\alpha$  is “Layout 1”, up to translation. Note that this gives the stabilisers of a surface code with uniform schedule, except the stabilisers have parallelogram shapes instead of square, just like in Section 2.1. We note that the  $NE^2N$ -stabilisers require the full connectivity of the square-grid architecture (Figure 1a). As another example with weight-4 stabilisers one may consider  $NESW$ -stabilisers, for which a quick calculation shows that all stabilisers are forced to be of the same type, so it cannot give rise to a quantum CSS code due to Theorem 1.

As another example, which this time gives a novel CSS code with weight-5 stabilisers, consider the  $NE^3N$ -stabilisers. We already established that  $\Delta(\vec{n}, \vec{e}, \vec{e}, \vec{e}, \vec{n})_{\text{odd}} = \{4\vec{e}, 6\vec{e} + 2\vec{n}\}$ , see Figure 6, and thus  $\mathcal{L} = \{2x(\vec{e} + \vec{n}) + 2y(\vec{e} - \vec{n}) : x, y \in \mathbb{Z}\}$ . Therefore, we have four sublattices for this case on which we are free to choose the value of the layout  $\alpha$ . In particular, we may choose the layouts from Figure 5. We point out that remarkably the syndrome extraction circuit of  $NE^3N$ -stabilisers uses only the hexagonal-grid connectivity (Figure 1b).

Now, we prove our theorem.

*Proof of Theorem 1.* We will consider everything in the data qubit sublattice’s frame of reference. Note then that the CPSWAP-version of conditions (a)–(c) remain the same, as the data qubits always move uniformly in one direction. So our goal from now on is to check against (a)–(c). Consider two ancilla qubits  $A_0, A'_0 \in \mathbb{Z}_{\text{anc}}^2$ , and the stabilisers they are associated with:  $\prod_{j=1}^w \alpha(A_0)_{Q_j}$  and  $\prod_{j=1}^w \alpha(A'_0)_{Q'_j}$ . Note that

$$\overrightarrow{Q_i Q'_j} = \overrightarrow{Q_i Q_j} + \overrightarrow{Q_j Q'_j} = \overrightarrow{A_0 A'_0} + \overrightarrow{Q_i Q_j} \text{ for all } i, j, \quad (8)$$

see (3) and Figure 7. Hence  $Q_i \neq Q'_i$ , therefore we conclude that (a) always holds, regardless of the layout  $\alpha$ .

Note that we only need to check (b)–(c) in case when  $\alpha(A) \neq \alpha(A')$ . From (8) we obtain

$$\{(i, j) : Q_i = Q'_j, i < j\} = \{(i, j) : \overrightarrow{Q_i Q_j} = -\overrightarrow{A_0 A'_0}, i < j\}. \quad (9)$$

Therefore, (b) is satisfied if and only if  $-\overrightarrow{A_0 A'_0} \notin \Delta_{\text{odd}}$ . By symmetry, we conclude that (c) holds if and only if  $\overrightarrow{A_0 A'_0} \notin \Delta_{\text{odd}}$ .

From the above observations we see that the layout  $\alpha$  gives a valid circuit if and only if

$$\alpha(A) = \alpha(A') \text{ holds for all } A, A' \in \mathbb{Z}_{\text{anc}}^2, \overrightarrow{AA'} \text{ or } -\overrightarrow{AA'} \in \Delta_{\text{odd}}. \quad (10)$$

This means that shifting the stabiliser by a vector or its opposite from  $\Delta_{\text{odd}}$  forces the same Pauli type on the two stabilisers. Clearly, if we shift again by another such vector, that third stabiliser is still forced to have the same Pauli type. Therefore, it is straightforward that we have a valid circuit if and only if (7) holds, which concludes the proof.  $\square$

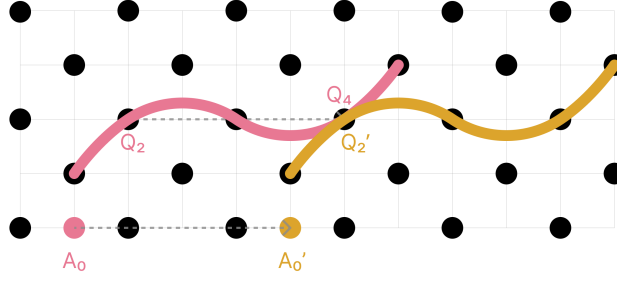


Figure 7: Two  $NE^3N$ -stabilisers in red and orange that are separated by the vector  $\overrightarrow{A_0 A_0'}$  which is in  $\Delta_{odd}$ . Hence by our theorem they are forced to have the same Pauli type. Note that  $\overrightarrow{A_0 A_0'} = \overrightarrow{Q_i Q_i'}$  for all  $i$ . Black dots are data qubits, the red and orange dots are the two ancilla qubits associated with the two shown stabilisers. The rest of the stabilisers and ancilla qubits are not shown.

Weight 4		
Direction	Valid Layouts	Connectivity
$NE^2N$	1	square-grid
Weight 5		
Direction	Valid Layouts	Connectivity
$NE^3N$	1,2,3	hex-grid
$NESEN$	1,2,3	hex-grid
$N^2EN^2$	1,2,3	hex-grid
Weight 6		
Direction	Valid Layouts	Connectivity
$NE^4N$	1	square-grid
$NEN^2EN$	1	square-grid
$NENWSW$	3	square-grid
$NES^2EN$	1	square-grid
$N^2E^2N^2$	1	square-grid

Weight 7		
Direction	Valid Layouts	Connectivity
$NE^5N$	1,2,3	hex-grid
$NE^3NEN$	1,2,3	hex-grid
$NE^2NE^2N$	1,2,3	square-grid
$NE^2SE^2N$	1,2,3	hex-grid
$NEN^3EN$	1,2,3	square-grid
$NENWEN$	1,2,3	hex-grid
$NESEEN$	1,2,3	square-grid
$NES^3EN$	1,2,3	square-grid
$NES^2WNE$	1	square-grid
$NESWSEN$	1,2,3	square-grid
$NESW^2NE$	1	square-grid
$N^2E^3N^2$	1,2,3	square-grid
$N^2ENEN^2$	1,2,3	square-grid
$N^2ESEN^2$	1,2,3	square-grid
$N^3EN^3$	1,2,3	square-grid

Table 1: All directions satisfying Theorem 1 with  $4 \leq w \leq 7$  and their valid layouts that give rise to CSS codes with equal numbers of  $X$ - and  $Z$ -stabilisers (after wrapping around a torus). Most of these require the full square-grid connectivity, but there are some that only use the hexagonal-grid.

Throughout our research we focused on CSS codes that are two-dimensional and have an equal number of  $X$ - and  $Z$ -stabilisers. For these we only encountered the three layouts from Figure 5. In Table 1 we list all the direction sequences between length 4 and 7 that can define such CSS codes when wrapped around a torus, which we discuss next in Section 2.4. We also included in Table 1 whether the circuit uses square- or hexagonal-grid connectivity. These direction sequences were found via an exhaustive search, where we assumed that the first direction is always  $\vec{n}$ , and the first direction after that which is different from it is  $\vec{e}$ . If one increases the length of the direction sequence further, one will find more CSS codes with even better encoding rates. However, as we increase the length we have a price to pay: the depth of the syndrome extraction circuit is increased, and hence it will become more noisy and potentially introduce more so-called bad hook errors [41–45].

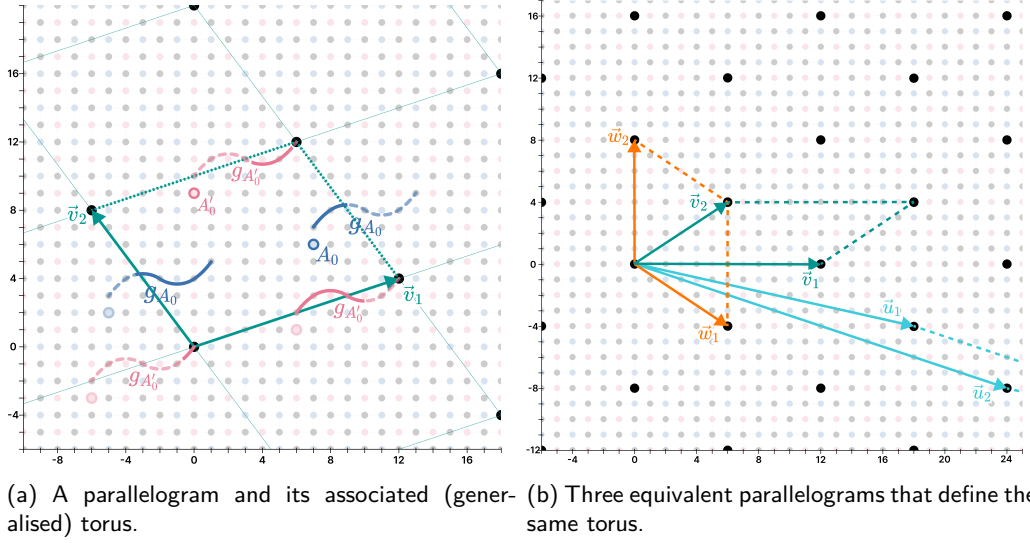


Figure 8: We show examples of parallelograms overlaid on the infinite plane, giving toric boundary conditions, as well as examples of equivalent parallelograms that thereby give equivalent code instances. (a) The parallelogram  $\mathcal{P}(\vec{v}_1 = (12, 4), \vec{v}_2 = (-6, 8))$  in green and its associated sublattice  $\mathcal{K}$  as large black points. This parallelogram with Layout 1 defines an  $NE^3N$ -code with four logical qubits. Two examples of  $NE^3N$ -stabilisers defined across the torus boundary are shown. Following the directions ordering,  $g_{A_0}$  in blue is the  $Z$  stabiliser associated with the starting ancilla qubit  $A_0$  located at  $(7, 6)$ , and is supported on data qubits  $(7, 7)$ ,  $(8, 8)$ ,  $(-2, 4) \equiv (10, 8) \pmod{\mathcal{K}}$ ,  $(0, 4) \equiv (12, 8) \pmod{\mathcal{K}}$  and  $(1, 5) \equiv (13, 9) \pmod{\mathcal{K}}$ . Similarly,  $g_{A'_0}$  in red is the  $X$  stabiliser associated with the starting ancilla qubit  $A'_0$  located at  $(0, 9)$ , and is supported on data qubits  $(6, 2)$ ,  $(7, 3)$ ,  $(9, 3)$ ,  $(5, 11) \equiv (11, 3) \pmod{\mathcal{K}}$ , and  $(0, 0) \equiv (6, 12) \equiv (12, 4) \pmod{\mathcal{K}}$ . (b) An example of three equivalent parallelograms:  $\mathcal{P}(\vec{v}_1 = (12, 0), \vec{v}_2 = (6, 4))$  in green,  $\mathcal{P}(\vec{w}_1 = (6, -4), \vec{w}_2 = (0, 8))$  in orange, and  $\mathcal{P}(\vec{u}_1 = (18, -4), \vec{u}_2 = (24, -8))$  in blue. Their associated (shared) sublattice  $\mathcal{K}$  is also shown as large black points.

## 2.4 Wrapping around parallelograms

So far we worked on an infinite plane and constructed a syndrome extraction circuit that measured an infinite number of stabilisers. In order to define a CSS code, we wrap the infinite plane, with the qubits and the stabilisers, around a parallelogram so that we obtain a CSS code on a (generalised) torus. Consider two linearly independent vectors  $\vec{v}_1, \vec{v}_2 \in \mathbb{Z}^2$ . We define the parallelogram associated with these vectors as follows, where  $O = (0, 0)$ ,

$$\mathcal{P} = \mathcal{P}(\vec{v}_1, \vec{v}_2) = \left\{ P \in \mathbb{Z}^2 : \overrightarrow{OP} = a\vec{v}_1 + b\vec{v}_2 \text{ with some } 0 \leq a < 1, 0 \leq b < 1 \right\}. \quad (11)$$

Consider the sublattice  $\mathcal{K} = \text{SPAN}_{\mathbb{Z}}(\{\vec{v}_1, \vec{v}_2\})$ . The (generalised) torus we obtain by wrapping around the parallelogram  $\mathcal{P}$  is defined to be the quotient  $\mathbb{Z}^2/\mathcal{K}$ . As such, two points  $A, B \in \mathbb{Z}^2$  are the same on the torus if and only if  $\overrightarrow{AB} \in \mathcal{K}$ , for which we introduce the notation  $A \equiv B \pmod{\mathcal{K}}$ . Figure 8a illustrates an example of how stabilisers defined on a parallelogram wrap around across its boundary. Now we prove a proposition that allows us to define a CSS code on a torus whose syndrome extraction circuit requires a square- or hexagonal-grid connectivity.

**Proposition 1.** *Consider a sequence of directions  $\vec{d}_1, \vec{d}_2, \dots, \vec{d}_w$ , a valid layout on the infinite plane  $\alpha: \mathbb{Z}_{anc}^2 \rightarrow \{X, Z\}$ , and a parallelogram  $\mathcal{P} = \mathcal{P}(\vec{v}_1, \vec{v}_2)$ . Assume that*

- (i)  $A \not\equiv Q \pmod{\mathcal{K}}$  for all  $A \in \mathbb{Z}_{anc}^2$  and  $Q \in \mathbb{Z}_{data}^2$ ,

- (ii)  $A \not\equiv A' \pmod{\mathcal{K}}$  for all  $A, A' \in \mathbb{Z}_{anc}^2$  and  $\alpha(A) \neq \alpha(A')$ ,
- (iii)  $\Delta \cap \mathcal{K} = \emptyset$ ,
- (iv) for any two delta vectors  $\vec{u}, \vec{w} \in \Delta$  we have  $\{\vec{u} - \vec{w}, \vec{u} + \vec{w}\} \cap \mathcal{K} \subseteq \{\vec{0}\}$ .

Let  $\mathcal{P}_{data} := \mathbb{Z}_{data}^2 \cap \mathcal{P}$ , and for each  $A_0 \in \mathcal{P}_{anc} := \mathbb{Z}_{anc}^2 \cap \mathcal{P}$  define the Pauli operator  $g_{A_0} := \prod_{j=1}^w \alpha(A_0)_{Q_j}$  where  $Q_j$  is defined in Equation (3). Then

$$\mathcal{S} = \mathcal{S}(\mathcal{P}; \alpha; \vec{d}_1, \vec{d}_2, \dots, \vec{d}_w) := \langle g_{A_0} : A_0 \in \mathcal{P}_{anc} \rangle \quad (12)$$

defines a CSS code on data qubits  $\mathcal{P}_{data}$ . Furthermore, the circuit  $\mathcal{C}(\alpha; \vec{d}_1, \vec{d}_2, \dots, \vec{d}_w)$  when considered on the torus achieves measuring all the stabilisers simultaneously and independently, and uses the set of qubits  $\mathcal{P}_{data} \cup \mathcal{P}_{anc}$ .

*Proof.* Conditions (i)–(ii) ensure that  $g_{A_0}$  is well-defined, and (iii) that the data qubits of any stabiliser are different. We will show that (iv) further implies that the circuit measures all the operators  $g_{A_0}$  simultaneously and independently, which implicitly implies that  $\mathcal{S}$  is Abelian. For this consider two operators  $g_{A_0} = \prod_{j=1}^w \alpha(A_0)_{Q_j}$  and  $g_{A'_0} = \prod_{j=1}^w \alpha(A'_0)_{Q'_j}$  such that  $A_0 \not\equiv A'_0 \pmod{\mathcal{K}}$ . Note that  $Q_j \not\equiv Q'_j \pmod{\mathcal{K}}$  for all  $j$ . Assume now that  $Q_i \equiv Q'_j \pmod{\mathcal{K}}$  for some  $i \neq j$ . Without loss of generality we may assume that  $Q_i = Q'_j$  as points on the plane. Note that for any indices  $k, \ell$  we have  $\overrightarrow{Q_k Q'_\ell} = \overrightarrow{Q_k Q'_i} + \overrightarrow{Q'_i Q'_\ell}$ . Since each vector on the right hand side is either a delta vector or its opposite is, we obtain from (iv) that  $Q_k \equiv Q'_\ell \pmod{\mathcal{K}}$  happens if and only if  $Q_k = Q'_\ell$ . Therefore, if the circuit measures all the operators simultaneously and independently on the plane, it does so also on the torus, which concludes the proof.  $\square$

As previously pointed out, we refer to such a CSS code on a (generalised) torus as a  $D_1 D_2 \dots D_w$ -code.

We define two parallelograms  $\mathcal{P}(\vec{v}_1, \vec{v}_2)$  and  $\mathcal{P}(\vec{w}_1, \vec{w}_2)$  to be equivalent if they define the same torus. Figure 8b shows an example. This happens if and only if the sublattices  $\text{SPAN}_{\mathbb{Z}}(\{\vec{v}_1, \vec{v}_2\})$  and  $\text{SPAN}_{\mathbb{Z}}(\{\vec{w}_1, \vec{w}_2\})$  are the same. We may write  $\vec{w}_i = \sum_{j=1}^2 \gamma_{ij} \vec{v}_j$  with some  $\gamma_{ij} \in \mathbb{R}$ , and define the matrix  $\Gamma := [\gamma_{ij}]_{i,j=1}^2 \in \mathbb{R}^{2 \times 2}$ . Note that  $\vec{v}_i = \sum_{j=1}^2 \beta_{ij} \vec{w}_j$  where  $\Gamma^{-1} = [\beta_{ij}]_{i,j=1}^2$ . We prove the following about the equivalence.

**Proposition 2.** *The parallelograms  $\mathcal{P}(\vec{v}_1, \vec{v}_2)$  and  $\mathcal{P}(\vec{w}_1, \vec{w}_2)$  are equivalent if and only if  $\Gamma$  has integer elements and its determinant is either  $-1$  or  $1$ .*

*Proof.* Clearly,  $\vec{w}_i \in \text{SPAN}_{\mathbb{Z}}(\{\vec{v}_1, \vec{v}_2\})$  happens if and only if both elements in the  $i$ th row of  $\Gamma$  are integers. Therefore,  $\text{SPAN}_{\mathbb{Z}}(\{\vec{w}_1, \vec{w}_2\}) \subseteq \text{SPAN}_{\mathbb{Z}}(\{\vec{v}_1, \vec{v}_2\})$  if and only if  $\Gamma \in \mathbb{Z}^{2 \times 2}$ . Note that because the two vectors in each pair are linearly independent, it follows that  $\Gamma$  is invertible in  $\mathbb{R}^{2 \times 2}$ . Thus, the reverse inclusion  $\text{SPAN}_{\mathbb{Z}}(\{\vec{v}_1, \vec{v}_2\}) \subseteq \text{SPAN}_{\mathbb{Z}}(\{\vec{w}_1, \vec{w}_2\})$  holds if and only if  $\Gamma^{-1} \in \mathbb{Z}^{2 \times 2}$ .

Because of the above, the two sublattices are the same if and only if  $\Gamma, \Gamma^{-1} \in \mathbb{Z}^{2 \times 2}$ . On the one hand, this latter implies that both  $\det \Gamma$  and  $\frac{1}{\det \Gamma}$  are integers, forcing  $\det \Gamma = \pm 1$ . On the other hand, if  $\Gamma \in \mathbb{Z}^{2 \times 2}$  and  $\det \Gamma = \pm 1$ , then  $\Gamma^{-1} = \frac{1}{\det \Gamma} \begin{bmatrix} \gamma_{22} & -\gamma_{12} \\ -\gamma_{21} & \gamma_{11} \end{bmatrix}$ , and as such it has integer elements, which concludes the proof.  $\square$

This proposition also ensures that if we wrap the circuit  $\mathcal{C}(\alpha; \vec{d}_1, \vec{d}_2, \dots, \vec{d}_w)$  around two equivalent parallelograms, then, given the conditions of Proposition 1 hold, we obtain the same circuit and associated CSS code.

### 3 Simulation results

We present numerical results here for three directional codes, namely, the  $NE^3N$ -code with four logical qubits, the  $N^2E^2N^2$ -code with six logical qubits, and the  $N^2E^3N^2$ -code with twelve logical qubits. These were picked based on some initial simulations, wherein we made heavy use of Proposition 2 to vastly reduce the number of parallelograms  $\mathcal{P}$  considered when searching over the possible CSS codes  $\mathcal{S}(\mathcal{P}; \alpha; \vec{d}_1, \vec{d}_2, \dots, \vec{d}_w)$ . For all of these directional codes the stabilisers are allocated according to  $\alpha = \text{“Layout 1”}$  (Figure 5a). In Appendix A we explain the structure of the logical operators of these three directional codes.

We compare the quantum memory performance of our novel CSS codes to the BB codes, and like in [28], we also compare them against the RPC, the current standard. We used BP-OSD [46–48] as our decoder for all experiments. We do this under the assumption of the standard superconducting-inspired circuit-level Pauli noise model from [49, 50], called “SI-1000”, which is parametrised by a parameter  $p$  called the physical error rate. We varied  $p$  between  $10^{-3}$  and  $10^{-2}$  for all experiments. We note that the SI-1000 noise model originally does not include the iSWAP gate, so we added the same noise after iSWAPs as after CZ gates. In this way the two entangling gates have the same amount of noise. Using this noise model we find that the directional codes outperform the RPC by using only 18.75 – 45% of the number of physical qubits to achieve approximately the same logical error probability. Although directional codes do not match the performance of the BB codes under this simple noise model, it is important to keep in mind that BB codes require degree-6 connectivity and long-range connections on the hardware, whereas directional codes have much more relaxed hardware requirements. This is discussed further in Section 4. All our circuits, as well as parity check matrices for each code, can be found in [51].

Before we present our numerical results, we point out that all results below use five QEC rounds, and are for just  $X$ -memory experiments, since the QEC performance of the two memory types is approximately the same. For the directional codes, this is because they have a symmetric layout of stabilisers, so shifting the logical  $X$ -operators by the vector  $(1, 1)$  gives the  $Z$ -logical operators. Further, the syndrome extraction circuit of these codes uses the same uniform schedule for both types of stabilisers. Hence, for each experiment we prepared the data qubits of the CSS code in the  $|+\rangle$  state, performed five rounds of syndrome extraction, measured out the data qubits in the  $X$ -basis and formed logical observables from all the logical  $X$ -operators of the CSS code. As for the BB codes and RPCs, it is well-known that the two memory types perform approximately the same [28, 44].

All our plots show the logical error probability per shot, denoted by  $p_L$ . More precisely, for all circuits we counted the number of shots for which any of the logical operators were not decoded correctly (across the five QEC rounds) and divided it by the total number of shots.

In Table 2, we provide a list of all directional codes for which we present detailed plots in this section, alongside with their  $\llbracket n, k, d \rrbracket$  parameters and the vectors specifying the parallelogram on which the codes were placed. We also show their net encoding rate, i.e. the ratio between the number of logical qubits and the total number of physical qubits (including the ancilla qubits), which is  $\frac{k}{2n}$  for directional codes. We note that Table 3 contains further directional codes for which we present detailed simulation results only in Appendix B.2. However, they are included in those plots here which show  $p_L$  against the total number of physical qubits at  $p = 10^{-3}$  (Figures 10, 12 and 14).



Directions	$\llbracket n, k, \leq d \rrbracket$	$\vec{v}_1$	$\vec{v}_2$	Net encoding rate
$NE^3N$	$\llbracket 36, 4, 4 \rrbracket$	(18, 0)	(0, 4)	$\frac{1}{18}$
$NE^3N$	$\llbracket 72, 4, 6 \rrbracket$	(18, 0)	(12, 8)	$\frac{1}{36}$
$NE^3N$	$\llbracket 120, 4, 8 \rrbracket$	(30, 0)	(6, 8)	$\frac{1}{60}$
$NE^3N$	$\llbracket 180, 4, 10 \rrbracket$	(30, 0)	(18, 12)	$\frac{1}{90}$
$N^2E^2N^2$	$\llbracket 64, 6, 4 \rrbracket$	(8, 0)	(0, 16)	$\frac{1}{21}$
$N^2E^2N^2$	$\llbracket 144, 6, 6 \rrbracket$	(12, 0)	(0, 24)	$\frac{1}{48}$
$N^2E^2N^2$	$\llbracket 256, 6, 8 \rrbracket$	(16, 0)	(0, 32)	$\frac{1}{85}$
$N^2E^3N^2$	$\llbracket 48, 12, 4 \rrbracket$	(12, 0)	(6, 8)	$\frac{1}{8}$
$N^2E^3N^2$	$\llbracket 144, 12, 6 \rrbracket$	(18, 0)	(12, 16)	$\frac{1}{24}$
$N^2E^3N^2$	$\llbracket 288, 12, 8 \rrbracket$	(24, 0)	(18, 24)	$\frac{1}{48}$

Table 2: The directional codes presented in this section, alongside with their parameters and their net encoding rates (rounded down to the nearest inverse integer). Note that all of their stabilisers are allocated according to “Layout 1”.

Further details on the simulations and additional results are available in Appendix B.

### 3.1 $NE^3N$ -codes encoding four logical qubits

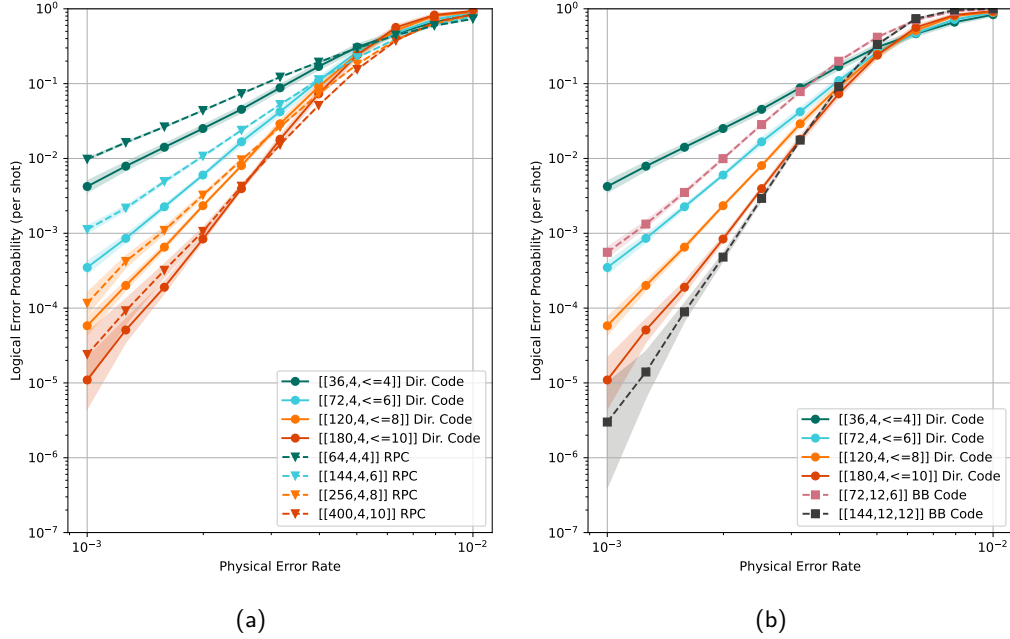


Figure 9: Comparison of  $NE^3N$ -codes to the RPC and BB codes under SI-1000 circuit-level Pauli noise. On both plots the scaling on the  $x$ - and  $y$ -axes are the same. The  $NE^3N$ -codes with parameters  $\llbracket \frac{3}{2}d^2 + 3d, 4, \leq d \rrbracket$  for  $d = 4, 6, 8, 10$  are depicted with solid green, blue, orange and red lines, respectively, all of them with a dot marker. (a)  $NE^3N$ -codes are compared against four copies of the RPC. Because of this the number of encoded logical qubits is four for both. The data for the RPC are shown with dashed lines and triangle markers. Their colours match the conjectured distances of the  $NE^3N$ -codes. (b)  $NE^3N$ -codes are compared against the  $\llbracket 72, 12, 6 \rrbracket$  and  $\llbracket 144, 12, 12 \rrbracket$  BB codes (dashed pink and black lines, respectively, with square markers). Note that these  $NE^3N$ -codes encode four logical qubits, while the BB codes encode twelve.

Figure 9 shows our numerical results for the  $NE^3N$ -codes, which encode four logical qubits, use only degree-3 connectivity hardware, and do not require any long-range connections. We picked four directional codes for our simulations with parameters  $\llbracket \frac{3}{2}d^2 + 3d, 4, \leq d \rrbracket$  for  $d = 4, 6, 8, 10$  (according to cases (a) and (b.2) in Appendix A.1), where the code distance is specified as an upper estimate. We also conjecture the effective (i.e. circuit-level) code distance to be  $d$  (see Appendix A.1 for more details), which the numerical results support as we see a clear exponential suppression for fixed  $p$  as we increase  $d$ .

In Figure 9a, we compare  $NE^3N$ -codes against four copies of the RPC. More precisely, we take the sampled logical failure probability  $p_L(1)$  corresponding to one RPC, and then apply the formula  $p_L := 1 - (1 - p_L(1))^4$  to get the logical failure probability corresponding to four independent RPCs, which is plotted. Therefore, in Figure 9a the number of encoded logical qubits is the same. These results are particularly encouraging as we achieve a lower logical failure probability at each code distance, and we are doing so using only  $\left(\frac{3}{8} + O\left(\frac{1}{d}\right)\right) \times$  the number of physical qubits. Therefore, the  $NE^3N$ -codes clearly outperform the RPC. For instance, at (conjectured) distance 10 the  $NE^3N$ -code’s net encoding rate is  $\approx 2.22\times$  that of the RPC. The plot shows that at  $p \approx 10^{-2.6}$  the two CSS codes achieve the same logical failure probability, and as  $p$  gets lower the  $NE^3N$ -code achieves lower  $p_L$ , with the gap between them increasing. Similar observations hold for the other distances.

In Figure 9b, we plot the logical error probability per shot for the  $NE^3N$ -codes, the smallest BB code with parameters  $\llbracket 72, 12, 6 \rrbracket$  and the gross code with parameters  $\llbracket 144, 12, 12 \rrbracket$  from [28]. Even though the BB codes encode twelve logical qubits, they require degree-6 connectivity hardware and two long-range connections per physical qubit. We see that at (conjectured) distance 6 the logical error probabilities are similar for the two codes, that of the  $NE^3N$ -code being slightly lower. From the plot we may extrapolate to (conjectured) distance 12, which suggests that a similar statement would be true. Therefore, taking into account the number of encoded logical qubits and the number of physical qubits used, the BB codes clearly outperform the  $NE^3N$ -codes. However, the “SI-1000” noise model (like similar commonly used noise models in the literature) does not take into account the additional noise that increasing the degree of connectivity or adding long-range connections would introduce on the hardware (see [15]). Therefore, the  $NE^3N$ -codes may be a better contender for hardware implementation. We note that recent attempts to implement long-range connections for BB codes on superconducting hardware have been somewhat successful [27], though several challenges remain regarding the error rates of both the long-range two-qubit gates and the logical qubits themselves.

In Figure 10, we again compare all of our  $NE^3N$ -codes (including also the ones from Table 3) against the RPC, this time fixing  $p = 10^{-3}$  and comparing the total number of qubits used, plotted on the  $x$ -axis, against the logical error probability, on the  $y$ -axis. We see that for a given total number of physical qubits, our codes outperform the RPC by providing in most cases at least an order of magnitude improvement in the logical error probability. Alternatively, directional codes use only 36.7 – 45% of the total number of physical qubits to achieve approximately the same logical error probability as the RPC. This suggests again that our novel CSS codes are promising candidates for reducing the overhead of fault-tolerant quantum computation in both the short and long term.

We note that Appendix A.1 contains more information about  $NE^3N$ -codes, in particular their logical operator structure. Furthermore, Appendix B.2 contains some further numerical results.

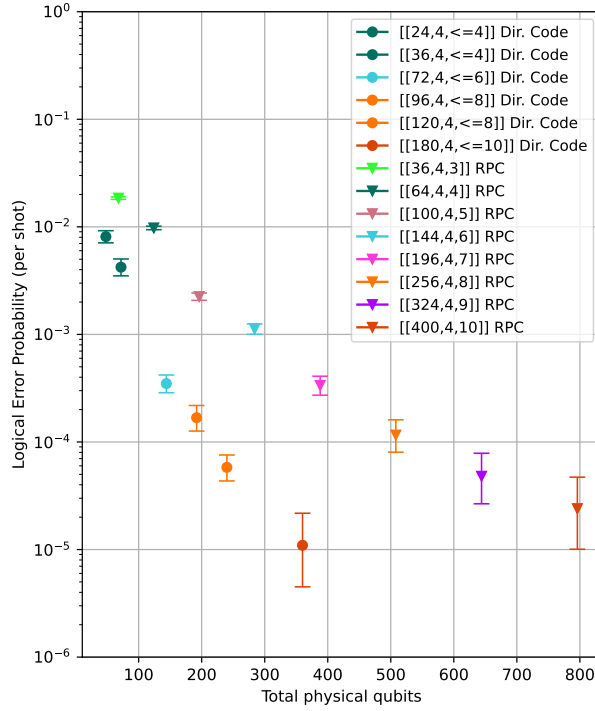


Figure 10: Comparison of the  $NE^3N$ -codes (from Tables 2 and 3) against the RPC where we fix  $p = 10^{-3}$  and plot the total number of physical qubits on the  $x$ -axis against the logical error probability per shot on the  $y$ -axis. The directional codes are marked with dots, and the RPCs with triangles. Each distance is assigned a unique colour, and codes of (conjectured) equal distance are plotted with the same colour.

### 3.2 $N^2E^2N^2$ -codes encoding six logical qubits

Our numerical results for  $N^2E^2N^2$ -codes, encoding six logical qubits, are shown in Figure 11. We picked three directional codes for our simulations with parameters  $\llbracket 4d^2, 6, \leq d \rrbracket$  for  $d = 4, 6, 8$ , see Appendix A.2 for more details. As in the  $NE^3N$  case, we conjecture the effective code distance to be exactly  $d$ . Comparing Figure 9 and Figure 11 shows that the exponential suppression of  $N^2E^2N^2$ -codes with six logical qubits is better than that of the  $NE^3N$ -codes with four logical qubits.

We also note that the gap between the logical failure probability of distance 4 and 6  $N^2E^2N^2$ -codes is bigger than between that of the distance 6 and 8 ones. We believe this is due to two reasons. First, the so-called “finite size” effect [12, 52], which is a common phenomenon where the state preparation and measurement (SPAM) errors affect the smaller distance codes more than the larger distance ones. Second, the error floor of the BP algorithm which has been studied extensively for classical codes, see e.g. [53]. We point out that this gap is also present in Figure 9, however, unlike for that case, we were unable to obtain numerical results for the distance 10  $N^2E^2N^2$ -code due to the size of the circuit.

In Figure 11a we compare the  $N^2E^2N^2$ -codes to the RPC, using a similar formula as in Section 3.1 to get a logical error probability for six independent RPCs. We see that the gap between the logical failure probabilities of the RPC and  $N^2E^2N^2$ -codes has widened significantly from the  $NE^3N$  case. The  $N^2E^2N^2$ -codes encode the same number of logical qubits as the RPC with using only  $\left(\frac{2}{3} + O\left(\frac{1}{d^2}\right)\right) \times$  the number of physical

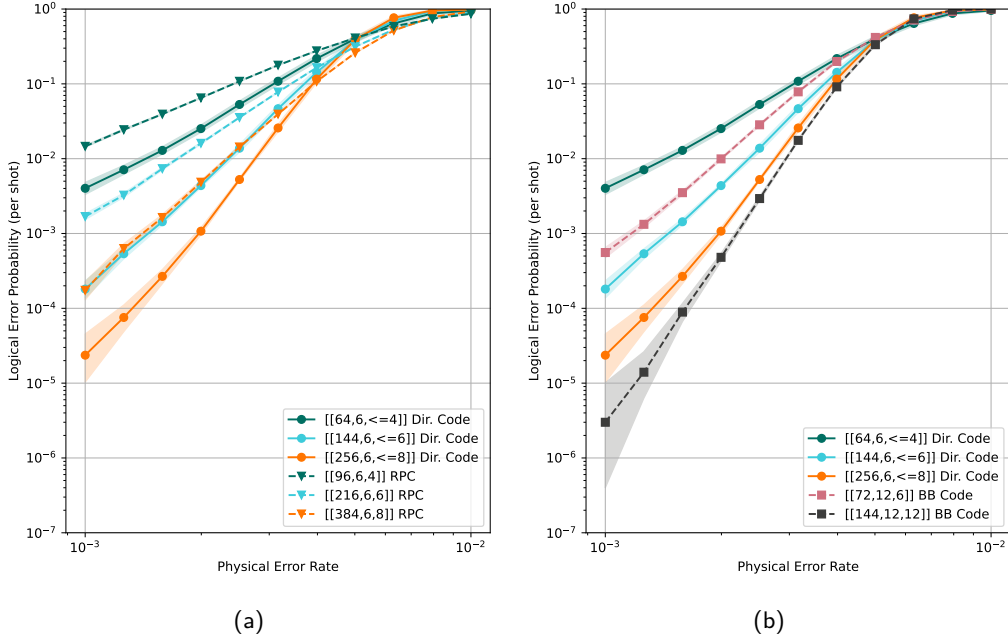


Figure 11: Comparison of  $N^2E^2N^2$ -codes to the RPC and BB codes under SI-1000 circuit-level Pauli noise. On both plots the scaling on the  $x$ - and  $y$ -axes are the same. The  $N^2E^2N^2$ -codes with parameters  $[[4d^2, 6, \leq d]]$  for  $d = 4, 6, 8$  are depicted with solid green, blue and orange lines, respectively, all of them with a dot marker. (a)  $N^2E^2N^2$ -codes are compared against six copies of the RPC, hence they both encode six logical qubits. The data for the RPC are shown with dashed lines and triangle markers. Their colours match the conjectured distances of the  $N^2E^2N^2$ -codes. (b)  $N^2E^2N^2$ -codes are compared against the  $[[72, 12, 6]]$  and  $[[144, 12, 12]]$  BB codes (dashed pink and black lines, respectively, with square markers). Note that these  $N^2E^2N^2$ -codes encode six logical qubits, while the BB codes encode twelve.

qubits. Furthermore, the (conjectured) distance 6  $N^2E^2N^2$ -code's graph overlaps with the distance 8 RPC's graph. From this we conclude that  $N^2E^2N^2$ -codes also outperform the RPC. Note that the  $N^2E^2N^2$ -codes presented here have net encoding rate  $\frac{3}{4d^2}$ , whereas the  $NE^3N$ -codes from Section 3.1 have net encoding rate  $\frac{4}{3d^2} + O\left(\frac{1}{d^3}\right)$ , which is higher. Therefore, even though the rate of exponential suppression is better for the  $N^2E^2N^2$  case, it is not entirely clear-cut which code has better QEC performance.

Figure 11b shows that the BB codes outperform the  $N^2E^2N^2$ -codes, however, similar to the  $NE^3N$  case, the  $N^2E^2N^2$ -codes are also competitive alternatives to BB codes, due to their relaxed connectivity requirements.

Similar to Figure 10, in Figure 12, we again compare all of our  $N^2E^2N^2$ -codes (including those from Table 3) against the RPC in terms of total qubit number at physical error rate  $p = 10^{-3}$ . We again see that for a given total number of physical qubits, our codes outperform the RPC, by providing in most cases one to two orders of magnitude improvement in the logical error probability. Alternatively, directional codes use only 24.49 – 42.66% of the total number of physical qubits to achieve approximately the same logical error probability as the RPC.

Appendix A.2 contains more information on  $N^2E^2N^2$ -codes, and Appendix B.2 further numerical results.

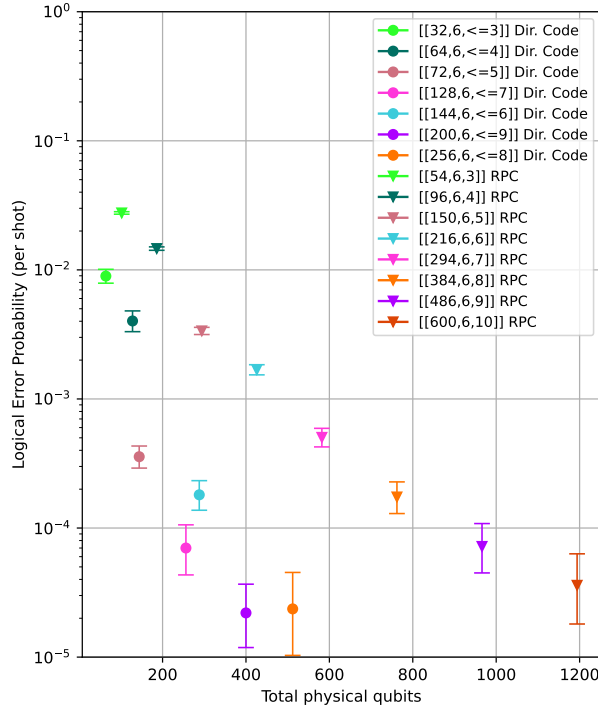


Figure 12: Comparison of the  $N^2E^2N^2$ -codes (from Tables 2 and 3) against the RPC where we fix  $p = 10^{-3}$  and plot the total number of physical qubits on the  $x$ -axis against the logical error probability per shot on the  $y$ -axis. The directional codes are marked with dots, and the RPCs with triangles. Each distance is assigned a unique colour, and codes of (conjectured) equal distance are plotted with the same colour.

### 3.3 $N^2E^3N^2$ -codes encoding twelve logical qubits

Figure 13 shows our numerical results for the  $N^2E^3N^2$ -codes which encode twelve logical qubits. We picked three directional codes with parameters  $\llbracket 6d^2 - 12d, 12, \leq d \rrbracket$  for  $d = 4, 6, 8$ , whose constructions are explained in Appendix A.3. Again,  $d$  is an upper estimate on the distance, but we conjecture the effective distance to be exactly  $d$ . As in the  $N^2E^2N^2$ -code case, the gap between distance 4 and 6 is bigger than between distance 6 and 8, which we again attribute to the finite size effect and the BP error floor. Comparing Figure 13 with Figures 9 and 11, we see that the exponential suppression of the  $N^2E^3N^2$ -codes with twelve logical qubits is comparable to that of the  $NE^3N$ - and  $N^2E^2N^2$ -codes.

In Figure 13a we compare the  $N^2E^3N^2$ -codes against twelve independent copies of the RPC, where our codes use only  $\left(\frac{1}{2} + O\left(\frac{1}{d}\right)\right) \times$  the number of physical qubits. Furthermore, the (conjectured) distance 6  $N^2E^3N^2$ -code has a steeper gradient than the distance 8 RPC, indicating even better performance at lower physical error rates. From this, we conclude that the  $N^2E^3N^2$ -codes also outperform the RPC.

Figure 13b shows that the BB codes also outperform the  $N^2E^3N^2$ -codes. However, the performance of the  $\llbracket 144, 12, \leq 6 \rrbracket$  directional code almost matches that of the smallest BB code at physical error rate  $p = 10^{-3}$ , using only twice as many qubits, and importantly without using any long range connections. Note that the gradient for the directional code is noticeably steeper, suggesting that at  $p = 10^{-4}$  physical error rate it would substantially outperform the smallest BB code. From the results we may also extrapolate and expect that the gradient of the (conjectured) distance 12  $N^2E^3N^2$ -code's gradient would

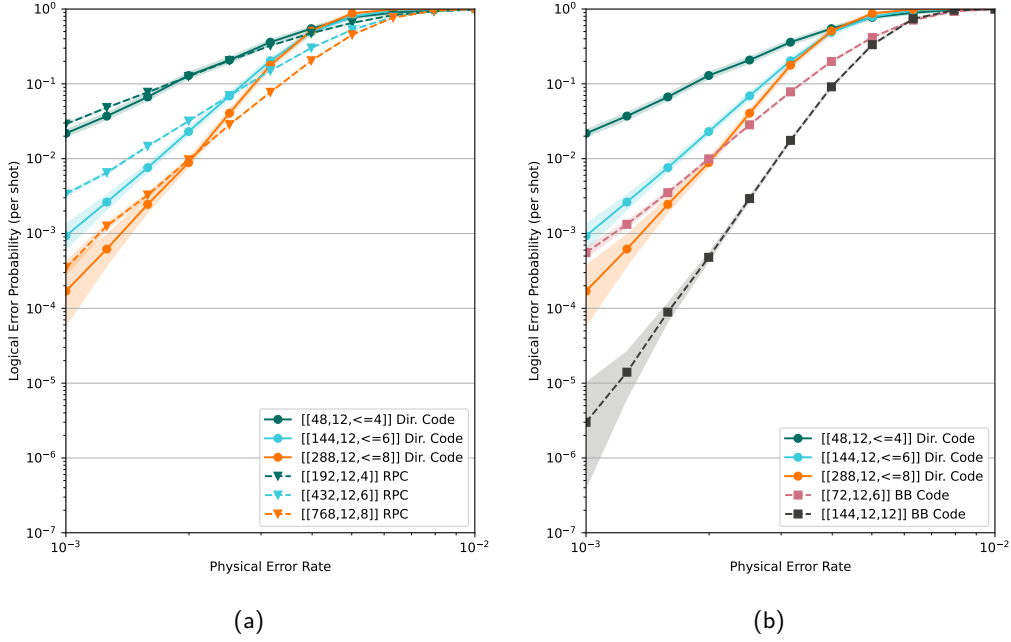


Figure 13: Comparison of  $N^2E^3N^2$ -codes to the RPC and BB codes under SI-1000 circuit-level Pauli noise. On both plots the scaling on the  $x$ - and  $y$ -axes are the same. The  $N^2E^3N^2$ -codes with parameters  $[[6d^2 - 12d, 12, d]]$  for  $d = 4, 6, 8$  are depicted with solid green, blue and orange lines, respectively, all of them with a dot marker. (a)  $N^2E^3N^2$ -codes are compared against twelve copies of the RPC. Because of this the number of encoded logical qubits is twelve for both. The data for the RPC are shown with dashed lines and triangle markers. Their colours match the conjectured distances of the  $N^2E^3N^2$ -codes. (b)  $N^2E^3N^2$ -codes are compared against the  $[[72, 12, 6]]$  and  $[[144, 12, 12]]$  BB codes (dashed pink and black lines, respectively, with square markers). Note that these  $N^2E^3N^2$ -codes encode twelve logical qubits, matching the BB codes.

be steeper than that of the  $[[144, 12, 12]]$  BB code (a.k.a the gross code). This makes the  $N^2E^3N^2$ -codes a very promising candidate for achieving low-overhead fault-tolerant quantum computing.

Similar to Figures 10 and 12, in Figure 14, we again compare all of our  $N^2E^3N^2$ -codes (including those from Table 3) against the RPC in terms of total qubit number at  $p = 10^{-3}$  physical error rate. We again see that for a given total number of physical qubits, directional codes outperform the RPC, by providing in most cases one to two orders of magnitude improvement in the logical error probability. Alternatively, our codes use only 18.75 – 25% of the total number of physical qubits to achieve approximately the same logical error probability as the RPC. Although we were unable to simulate larger codes, we anticipate that this pattern continues, providing substantial reductions in the number of physical qubits required to encode a high number of logical qubits on near-term square-grid hardware.

Appendix A.3 contains more information on  $N^2E^3N^2$ -codes, and Appendix B.2 further numerical results.

## 4 Discussion

In this paper, we present a novel family of qLDPC codes that can be implemented under relaxed hardware requirements, namely, with square-grid and hexagonal-grid connectivity. We simulated three families of directional codes with four, six and twelve logical qubits,



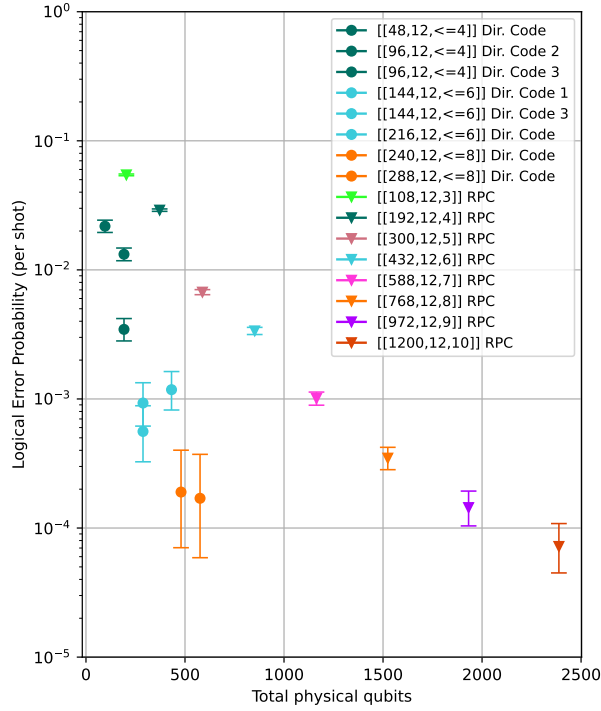


Figure 14: Comparison of the  $N^2E^3N^2$ -codes (from Tables 2 and 3) against the RPC where we fix  $p = 10^{-3}$  and plot the total number of physical qubits on the  $x$ -axis against the logical error probability per shot on the  $y$ -axis. The directional codes are marked with dots, and the RPCs with triangles. Each distance is assigned a unique colour, and codes of (conjectured) equal distance are plotted with the same colour. In the case where two codes have the same qubit number, the code belonging to the “no-pattern” family (3) (see Appendix B.2) is the better performing of the two. Note that the  $[[384, 12, \leq 8]]$  code from family (3) (see Appendix B.2) is not shown, as we did not simulate it at  $p = 10^{-3}$ .

and found that they outperform the RPC under circuit-level Pauli noise, both in terms of logical fidelity and encoding rate. We also found that directional codes do not outperform BB codes, however it is important to note that this assumed a somewhat simplistic circuit-level Pauli noise model which does not introduce additional noise into the system with increased connectivity and long-range connections. Since on a physical hardware both of these modifications – that our CSS codes do not need – introduce additional noise and engineering challenges, directional codes may be a potentially more desirable choice than the BB codes for hardware implementation.

Our main idea was to utilise iSWAP gates instead of CZ gates to implement the syndrome-extraction circuits of directional codes. Since iSWAP gates essentially dynamically alter the connectivity, utilising them opens up a new way to discover better QEC codes than the ones which use the more popular CZ gate. For instance, we believe that using the ideas developed here, it may be possible to construct novel qLDPC codes that can be implemented on the same hardware that the BB codes require (see also Equation (13) below). This we leave as an interesting open question.

We see two potential ways for directional codes to really challenge BB codes in the long-term under relaxed connectivity requirements. Note that similarly to the BB codes, here we defined directional codes on a torus. Therefore, the first potential way is to develop a modular quantum computer similar to what is described in IBM’s “Tour de Gross” roadmap [18]. More precisely, similarly to [18, Figure 6], a directional code could

be stored on each toric “code module”, and the planar “factory module” could operate with RPCs. The other potential future way would be to first add boundaries to directional codes, so that they can be implemented on a planar hardware. Then the next natural step would be to develop the analogue of lattice surgery for planar directional codes. Finally, it needs to be figured out how to prepare high-quality magic states, which may be by using planar directional codes or RPCs. This would make it possible to perform logical circuits via the Pauli-based computational model [54]. We believe this latter option is more promising, as it only requires the scaling up of the square-grid architecture with iSWAP gates. Also the latter option does not require purpose-built hardware, but one that can be general-purpose, accommodating various QEC codes.

Recent improvements in BP-based decoders, especially [55], suggest that expensive and slow post-processing steps, like OSD, may not be necessary for real-time decoding of qLDPC codes. Our directional codes were decoded with BP-OSD [46], therefore we anticipate they will be compatible also with BP-relay [55]. Alternatively, there may be scope for development of a bespoke decoder for directional codes, which we leave as an interesting open problem.

In the paper we focused on implementing directional codes using iSWAP gates, which is a natural native gate on superconducting qubits. We note that iSWAP is also natural on spin qubits, though the connectivity is less restricted on them [56, 57], making them a good option on such platforms too. Further to that, first we point out that directional codes can also be implemented on AMO hardware. Due to the shape of their stabilisers, the directional codes presented in Section 3 require the qubits to be moved/shuttled across shorter spatial distances than the BB codes, which may make them promising candidates even for AMO hardware. Second, note the following identity

$$\text{CXSWAP}(Q_0, Q_1)|\psi\rangle = \text{CX}(Q_0, Q_1)\text{CX}(Q_1, Q_0)|\psi\rangle. \quad (13)$$

Equation (13) clearly implies that directional codes can be implemented on solid state hardware even without iSWAP gates and the need to modify the connectivity, although the number of two-qubit gates is obviously doubled.

To summarise, our directional codes open up new avenues for achieving low-overhead fault-tolerant quantum computation without the use of long-range connections and increased connectivity hardware. We hope our codes inspire a new wave of ideas in the field leading to useful quantum computing sooner.

## Author Contributions

G.G. conceived the project idea and lead the project and paper writing. All authors contributed to the scientific work afterwards, as well as to software work. DB handled all the simulations and numerical data collection. All authors contributed to writing the paper.

## Acknowledgements

We would like to thank Dan Browne and Ophelia Crawford for reading an early version of the paper and providing valuable feedback. We also would like to thank Earl T. Campbell for some very inspiring discussions at the early stages of the project, and for creating a stimulating scientific environment at Riverlane. We are also grateful to Ophelia Crawford who leads the Logic team at Riverlane, and who was very supportive of the project from

the start and gave us space to work on it. We are also extremely grateful to Chidi Nnadi, Gordon Bateman and Mohamed Rashid Hassan, who provided us with a high performance computing cluster with hundreds of cores, without which this research would have been impossible. Finally, we thank Maria Maragkou and Luigi Martiradonna for giving feedback on the abstract, and the Introduction and Discussion sections.

## Corresponding authors

Correspondence and requests for materials should be addressed to G.G.  
([george.geher@riverlane.com](mailto:george.geher@riverlane.com), [gehergyuri@gmail.com](mailto:gehergyuri@gmail.com)) and D.B.  
([david.byfield@riverlane.com](mailto:david.byfield@riverlane.com), [david.s.byfield@gmail.com](mailto:david.s.byfield@gmail.com)).

## References

- [1] Richard P. Feynman. “Quantum mechanical computers”. *Foundations of Physics* **16**, 507–531 (1986).
- [2] Michael A. Nielsen and Isaac L. Chuang. “Quantum computation and quantum information: 10th anniversary edition”. Cambridge University Press. (2010).
- [3] John Preskill. “Quantum Computing in the NISQ era and beyond”. *Quantum* **2**, 79 (2018).
- [4] P.W. Shor. “Algorithms for quantum computation: discrete logarithms and factoring”. In Proceedings 35th Annual Symposium on Foundations of Computer Science. Pages 124–134. (1994).
- [5] Earl T. Campbell, Barbara M. Terhal, and Christophe Vuillot. “Roads towards fault-tolerant universal quantum computation”. *Nature* **549**, 172–179 (2017).
- [6] Barbara M. Terhal. “Quantum error correction for quantum memories”. *Rev. Mod. Phys.* **87**, 307–346 (2015).
- [7] Joschka Roffe. “Quantum error correction: an introductory guide”. *Contemporary Physics* **60**, 226–245 (2019). [arXiv:https://doi.org/10.1080/00107514.2019.1667078](https://doi.org/10.1080/00107514.2019.1667078).
- [8] Dorit Aharonov and Michael Ben-Or. “Fault-tolerant quantum computation with constant error rate”. *SIAM Journal on Computing* **38**, 1207–1282 (2008). [arXiv:https://doi.org/10.1137/S0097539799359385](https://doi.org/10.1137/S0097539799359385).
- [9] Emanuel Knill, Raymond Laflamme, and Wojciech H. Zurek. “Resilient quantum computation”. *Science* **279**, 342–345 (1998). [arXiv:https://www.science.org/doi/pdf/10.1126/science.279.5349.342](https://www.science.org/doi/pdf/10.1126/science.279.5349.342).
- [10] A.Yu. Kitaev. “Fault-tolerant quantum computation by anyons”. *Annals of Physics* **303**, 2–30 (2003).
- [11] Google Quantum AI. “Suppressing quantum errors by scaling a surface code logical qubit”. *Nature* **614**, 676–681 (2023).
- [12] Google Quantum AI and Collaborators. “Quantum error correction below the surface code threshold”. *Nature* **638**, 920–926 (2025).
- [13] Hany Ali, Jorge Marques, et al. “Reducing the error rate of a superconducting logical qubit using analog readout information”. *Phys. Rev. Appl.* **22**, 044031 (2024).
- [14] Laura Caune, Luka Skoric, Nick S. Blunt, et al. “Demonstrating real-time and low-latency quantum error correction with superconducting qubits” (2024). [arXiv:2410.05202](https://arxiv.org/abs/2410.05202).
- [15] Alec Eickbusch et al. “Demonstrating dynamic surface codes” (2025). [arXiv:2412.14360](https://arxiv.org/abs/2412.14360).
- [16] Joan Camps et al. “Leakage mobility in superconducting qubits as a leakage reduction unit” (2024). [arXiv:2406.04083](https://arxiv.org/abs/2406.04083).
- [17] “Google Quantum AI Roadmap”. <https://quantumai.google/roadmap>. Accessed: 2025-07-09.
- [18] Theodore J. Yoder et al. “Tour de gross: A modular quantum computer based on bivariate bicycle codes” (2025). [arXiv:2506.03094](https://arxiv.org/abs/2506.03094).
- [19] Bence Hetényi and James R. Wootton. “Creating entangled logical qubits in the heavy-hex lattice with topological codes”. *PRX Quantum* **5**, 040334 (2024).
- [20] Austin G. Fowler, Matteo Mariantoni, John M. Martinis, and Andrew N. Cleland. “Surface codes: Towards practical large-scale quantum computation”. *Phys. Rev. A* **86**, 032324 (2012).
- [21] Austin G. Fowler, Ashley M. Stephens, and Peter Groszkowski. “High-threshold universal quantum computation on the surface code”. *Phys. Rev. A* **80**, 052312 (2009).

- [22] Maxime A. Tremblay, Nicolas Delfosse, and Michael E. Beverland. “Constant-overhead quantum error correction with thin planar connectivity”. *Phys. Rev. Lett.* **129**, 050504 (2022).
- [23] Daniel Gottesman. “Fault-tolerant quantum computation with constant overhead” (2014). [arXiv:1310.2984](#).
- [24] Nikolas P. Breuckmann and Jens Niklas Eberhardt. “Quantum low-density parity-check codes”. *PRX Quantum* **2** (2021).
- [25] Pavel Panteleev and Gleb Kalachev. “Asymptotically good quantum and locally testable classical ldpc codes”. In Proceedings of the 54th Annual ACM SIGACT Symposium on Theory of Computing. *Page 375–388*. STOC 2022 New York, NY, USA (2022). Association for Computing Machinery.
- [26] Anthony Leverrier and Gilles Zémor. “Quantum tanner codes”. In 2022 IEEE 63rd Annual Symposium on Foundations of Computer Science (FOCS). *Pages 872–883*. (2022).
- [27] Ke Wang, Zhide Lu, Chuanyu Zhang, et al. “Demonstration of low-overhead quantum error correction codes” (2025). [arXiv:2505.09684](#).
- [28] Sergey Bravyi, Andrew W. Cross, Jay M. Gambetta, Dmitri Maslov, Patrick Rall, and Theodore J. Yoder. “High-threshold and low-overhead fault-tolerant quantum memory”. *Nature* **627**, 778–782 (2024).
- [29] Min Ye and Nicolas Delfosse. “Quantum error correction for long chains of trapped ions” (2025). [arXiv:2503.22071](#).
- [30] Mackenzie H. Shaw and Barbara M. Terhal. “Lowering connectivity requirements for bivariate bicycle codes using morphing circuits”. *Phys. Rev. Lett.* **134**, 090602 (2025).
- [31] Matt McEwen, Dave Bacon, and Craig Gidney. “Relaxing Hardware Requirements for Surface Code Circuits using Time-dynamics”. *Quantum* **7**, 1172 (2023).
- [32] S. A. Caldwell, N. Didier, C. A. Ryan, E. A. Sete, et al. “Parametrically activated entangling gates using transmon qubits”. *Phys. Rev. Appl.* **10**, 034050 (2018).
- [33] Youngkyu Sung et al. “Realization of high-fidelity cz and zz-free iswap gates with a tunable coupler”. *Phys. Rev. X* **11**, 021058 (2021).
- [34] Marco Roth et al. “Analysis of a parametrically driven exchange-type gate and a two-photon excitation gate between superconducting qubits”. *Phys. Rev. A* **96**, 062323 (2017).
- [35] R. Barends, J. Kelly, et al. “Superconducting quantum circuits at the surface code threshold for fault tolerance”. *Nature* **508**, 500–503 (2014).
- [36] M.A. Rol et al. “Fast, high-fidelity conditional-phase gate exploiting leakage interference in weakly anharmonic superconducting qubits”. *Physical Review Letters* **123** (2019).
- [37] R. Barends, C.M. Quintana, A.G. Petukhov, et al. “Diabatic gates for frequency-tunable superconducting qubits”. *Physical Review Letters* **123** (2019).
- [38] B. Foxen, C. Neill, A. Dunsworth, et al. “Demonstrating a continuous set of two-qubit gates for near-term quantum algorithms”. *Physical Review Letters* **125** (2020).
- [39] Youngkyu Sung et al. “Realization of high-fidelity cz and zz-free iswap gates with a tunable coupler”. *Phys. Rev. X* **11**, 021058 (2021).
- [40] Google Quantum AI. “Exponential suppression of bit or phase errors with cyclic error correction”. *Nature* **595**, 383–387 (2021).
- [41] György P. Gehér, Ophelia Crawford, and Earl T. Campbell. “Tangling schedules eases hardware connectivity requirements for quantum error correction”. *PRX Quantum* **5**, 010348 (2024).

- [42] Eric Dennis, Alexei Kitaev, Andrew Landahl, and John Preskill. “Topological quantum memory”. *Journal of Mathematical Physics* **43**, 4452–4505 (2002).
- [43] Yu Tomita and Krysta M. Svore. “Low-distance surface codes under realistic quantum noise”. *Phys. Rev. A* **90**, 062320 (2014).
- [44] Anthony Ryan O’Rourke and Simon Devitt. “Compare the pair: Rotated vs. unrotated surface codes at equal logical error rates” (2024). [arXiv:2409.14765](https://arxiv.org/abs/2409.14765).
- [45] György P. Gehér, Campbell McLauchlan, Earl T. Campbell, et al. “Error-corrected Hadamard gate simulated at the circuit level”. *Quantum* **8**, 1394 (2024).
- [46] Joschka Roffe, David R. White, Simon Burton, and Earl Campbell. “Decoding across the quantum low-density parity-check code landscape”. *Phys. Rev. Res.* **2**, 043423 (2020).
- [47] Oscar Higgott et al. “Improved decoding of circuit noise and fragile boundaries of tailored surface codes”. *Phys. Rev. X* **13**, 031007 (2023).
- [48] Pavel Panteleev and Gleb Kalachev. “Degenerate Quantum LDPC Codes With Good Finite Length Performance”. *Quantum* **5**, 585 (2021).
- [49] Craig Gidney, Michael Newman, Austin Fowler, and Michael Broughton. “A Fault-Tolerant Honeycomb Memory”. *Quantum* **5**, 605 (2021).
- [50] Craig Gidney, Michael Newman, Peter Brooks, and Cody Jones. “Yoked surface codes”. *Nat. Commun.* **16**, 4498 (2025).
- [51] György Pál Gehér, David Byfield, and Archibald Ruban. “Stim circuits and parity check matrices for ”directional codes: a new family of quantum ldpc codes on hexagonal- and square-grid connectivity hardware” manuscript” (2025). Available at <https://zenodo.org/doi/10.5281/zenodo.16422162>.
- [52] Craig Gidney and Martin Ekerå. “How to factor 2048 bit RSA integers in 8 hours using 20 million noisy qubits”. *Quantum* **5**, 433 (2021).
- [53] Tom Richardson. “Error floors of ldpc codes” (2003).
- [54] Sergey Bravyi, Graeme Smith, and John A. Smolin. “Trading classical and quantum computational resources”. *Phys. Rev. X* **6**, 021043 (2016).
- [55] Tristan Müller et al. “Improved belief propagation is sufficient for real-time decoding of quantum memory” (2025). [arXiv:2506.01779](https://arxiv.org/abs/2506.01779).
- [56] Jurgen Dijkema et al. “Cavity-mediated iswap oscillations between distant spins”. *Nature Physics* **21**, 168–174 (2024).
- [57] Guido Burkard et al. “Semiconductor spin qubits”. *Rev. Mod. Phys.* **95**, 025003 (2023).
- [58] Craig Gidney. “Stim: a fast stabilizer circuit simulator”. *Quantum* **5**, 497 (2021).
- [59] Oscar Higgott. “Stimbposd”. <https://github.com/oscarhiggott/stimbposd> (2024). Accessed: 2025-06-06.
- [60] Stasiu Wolanski and Ben Barber. “Ambiguity clustering: an accurate and efficient decoder for qldpc codes” (2025). [arXiv:2406.14527](https://arxiv.org/abs/2406.14527).
- [61] Timo Hillmann, Lucas Berent, et al. “Localized statistics decoding: A parallel decoding algorithm for quantum low-density parity-check codes” (2024). [arXiv:2406.18655](https://arxiv.org/abs/2406.18655).
- [62] Kai R. Ott, Bence Hetényi, and Michael E. Beverland. “Decision-tree decoders for general quantum ldpc codes” (2025). [arXiv:2502.16408](https://arxiv.org/abs/2502.16408).
- [63] Laleh Aghababae Beni, Oscar Higgott, and Noah Shutt. “Tesseract: A search-based decoder for quantum error correction” (2025). [arXiv:2503.10988](https://arxiv.org/abs/2503.10988).



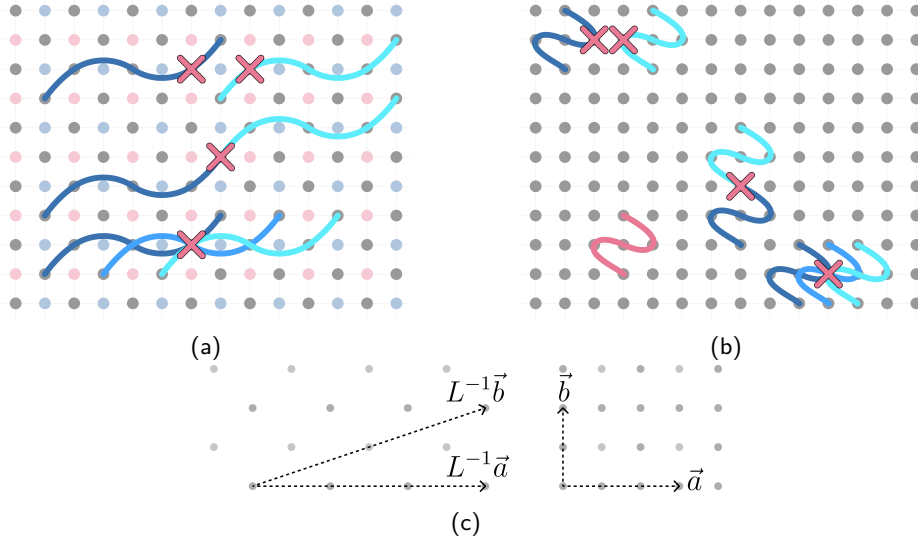


Figure 15: (a) Special type of errors for  $NE^3N$ -codes with “Layout 1”. The bottom case is an  $X$ -error happening just before the entangling layers of the QEC round, flipping three  $Z$ -stabiliser outcomes. The middle is similar but the  $X$ -error on that data qubit flips only two  $Z$ -stabilisers. The top case is the only  $XX$ -error on next-nearest neighbour qubits that flips two  $Z$ -stabilisers. (b) Linear transformed version, using the mapping  $L$ , of (a) where only the data qubits are shown. All the stabilisers from (a) are shown, together with an additional  $X$ -stabiliser. Notice that with this version the stabilisers whose outcomes are flipped due to an  $X$ - or  $XX$ -error shown here are aligned horizontally or vertically, which is why we use this transformed version for our discussion. (c) The vectors  $\vec{a}$ ,  $\vec{b}$  and their inverse images with respect to the linear mapping  $L$ . The grey dots correspond to the data qubits, ancilla qubits are not shown.

## A Logical operator structure

In this section of the appendix we give more insight into the structure of logical operators of the best directional codes we found and presented numerical results for in Section 3. Based on that, we conjecture that all of these codes scale quadratically in the number of qubits as the effective (i.e. circuit-level) distance increases. Recall that the stabilisers of all the directional codes discussed here are laid out according to “Layout 1” (Figure 5a). We note that for directional codes, the number of encoded logical qubits depends on the choice of the parallelogram  $\mathcal{P}$ . For all the codes we present in this paper we chose  $\mathcal{P}$  so that they encode the maximum number of logical qubits.

### A.1 $NE^3N$ -codes encoding four logical qubits

For each data qubit consider an  $X$ -error that happens just before we start the first entangling layer of the QEC round. Depending on where this data qubit is, the bit-flip error flips the outcomes of two or three  $Z$ -stabilisers. More precisely, if a data qubit is in the same row of qubits as an  $X$ -ancilla qubit, then two outcomes are flipped, otherwise three. A similar observation holds with  $Z$ -errors, namely if a data qubit is in the same row of qubits as a  $Z$ -ancilla qubit the error flips the outcome of two  $X$ -stabilisers, otherwise three. From this we can also see that the only way a correlated  $XX$ -error flips two  $Z$ -stabiliser outcomes on next-nearest neighbour data qubits is when they lie in a row which contains  $Z$ -ancillas, see Figure 15(a).

For our discussion we find it more convenient to apply the following linear transforma-

tion on  $\mathbb{Z}^2$

$$L: (2, 0) \mapsto (1, 0) \text{ and } (3, 1) \mapsto (0, 1). \quad (14)$$

In this way the data qubit sublattice  $\mathbb{Z}_{data}^2$  is mapped onto  $\mathbb{Z}^2$ . Note that the ancilla qubit sublattice  $\mathbb{Z}_{anc}^2$  is mapped onto a shifted square grid whose  $x$ -coordinates are not integers, but they will not be used for our discussion so we ignore them from now on. The shape of stabilisers change according to the mapping  $L$  as depicted in Figure 15b. Notice that we have alternating rows of  $X$ - and  $Z$ -stabilisers. From now until the end of the subsection we consider this transformed version of the layout.

Notice that the stabilisers whose outcomes are flipped due to the shown error mechanisms in Figure 15b are now horizontally or vertically aligned. Namely, in the top case we can shift the left-hand side stabiliser by the vector  $\vec{a} := (3, 0)$  to get the right-hand side stabiliser. Furthermore, in the middle case, if we shift the bottom stabiliser by  $\vec{b} = (0, 2)$  we obtain the top one.

During our investigation we found that the best performing  $NE^3N$ -codes of (conjectured) even distance  $d$  are the following:

- (a) For  $4 \mid d+2$ ,  $\vec{v}_1 := \frac{d}{2}\vec{a}$  and  $\vec{v}_2 := -\frac{d+2}{4}\vec{a} + \left(\frac{d}{2} + 1\right)\vec{b}$ . This gives a  $\left[\left[\frac{3}{2}d^2 + 3d, 4, \leq d\right]\right]$  CSS code.
- (b.1) For  $4 \mid d$ , we have two cases. The first one is when  $\vec{v}_1 := \frac{d}{2}\vec{a}$  and  $\vec{v}_2 := -\frac{d}{4}\vec{a} + \frac{d}{2}\vec{b}$ , giving a  $\left[\left[\frac{3}{2}d^2, 4, \leq d\right]\right]$  CSS code.
- (b.2) The other case for  $4 \mid d$  is when  $\vec{v}_1 := \left(\frac{d}{2} + 1\right)\vec{a}$  and  $\vec{v}_2 := -\left(\frac{d}{4} + 1\right)\vec{a} + \frac{d}{2}\vec{b}$  that gives a  $\left[\left[\frac{3}{2}d^2 + 3d, 4, \leq d\right]\right]$  CSS code.

In Section 3.1 we showed results for (a) and (b.2), because the first two code parameters for them are the same, and the logical error probabilities for (b.1) are slightly higher than that of (b.2). In Appendix B.2 we present numerical results for the (b.1) case, see Figure 21. Note that (b.1) uses  $O(d)$  less qubits than (b.2), which is negligible for large  $d$ . However, when aiming for a small distance hardware demonstration, this slight difference could matter, especially when there is a restriction on the number of physical qubits.

Consider the case of (a), and assume that the qubit at  $(0, 0)$  is the middle qubit of an  $X$ -stabiliser (or equivalently is where a  $Z$ -stabiliser starts), as depicted in Figure 16 for the  $d = 10$  case. Due to the structure of the parallelogram, each row of qubits is a cycle on the torus containing  $3\frac{d}{2}$  qubits. Based on the observations we made earlier for Figure 15, if we arrange  $\frac{d}{2}$   $XX$ -errors in a horizontal row with odd  $y$ -coordinate and leaving a gap of one qubit between them, we obtain a Pauli- $X$  operator of weight  $d$  that commutes with all stabilisers, e.g.

$$\hat{X}_1 := \prod_{\ell=0}^{\frac{d}{2}-1} X_{(3\ell-1,1)} X_{(3\ell,1)} \quad \text{and} \quad \hat{X}_2 := \prod_{\ell=0}^{\frac{d}{2}-1} X_{(3\ell+1,1)} X_{(3\ell+2,1)}. \quad (15)$$

Notice that shifting  $\hat{X}_1$  by the vector  $(-1, 0)$  gives us  $\hat{X}_2$ , and shifting  $\hat{X}_1$  by  $(1, 0)$  gives  $\hat{X}_1 \hat{X}_2$ , both up to stabiliser equivalence. Furthermore, shifting any of these operators by an integer multiple of  $\vec{b}$  gives the same operator up to stabiliser equivalence. However, as we will see later,  $\hat{X}_1$  and  $\hat{X}_2$  are not equivalent to each other.

Instead of arranging  $X$ -errors horizontally, we could arrange single  $X$ -errors vertically in a cycle and leaving a gap of 1 qubit between them. If we started from any data qubit with even  $x$ - and  $y$ -coordinates, this would give us an  $X$ -Pauli string of weight  $\frac{d}{2} \left(\frac{d}{2} + 1\right)$

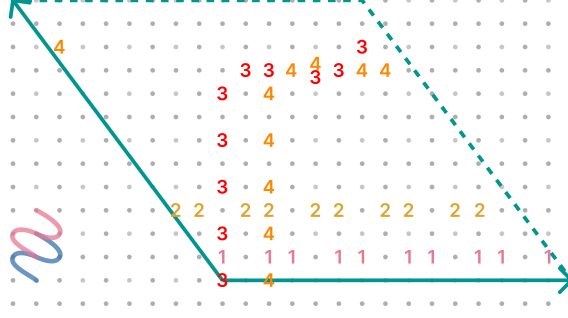


Figure 16: Illustration of the  $X$ -logical operators of the  $NE^3N$ -code with parameters specified in (a) with  $d = 10$ , i.e.  $\vec{v}_1 = 5\vec{a}$  and  $\vec{v}_2 = -3\vec{a} + 6\vec{b}$  (green solid vectors). The logical operators defined in the text,  $\hat{X}_1, \hat{X}_2, \hat{X}_3, \hat{X}_4$  are depicted as a string of numbers corresponding to their indices, each coloured with a distinct colour. The  $Z$ -logical operators  $\hat{Z}_1, \hat{Z}_2, \hat{Z}_3, \hat{Z}_4$  can be obtained by translating their  $X$  counter part by the vector  $(0, 1)$  and changing the Pauli terms to  $Z$ s. An  $X$ - and a  $Z$ -stabiliser (outside the torus) are also shown for reference.

that commutes with all stabilisers. However, we can find Pauli- $X$  strings of lower weight that commutes with all stabilisers if we combine horizontal and vertical  $XX$ - and  $X$ -errors to create a shorter cycle. More precisely, a product of  $\frac{d}{2} + 1$  weight-one  $X$ -errors arranged vertically can be made a cycle if we join its two ends by  $\frac{d-2}{4}$  weight-two  $XX$ -errors arranged horizontally. This gives the following  $X$ -string of weight  $d$ :

$$\hat{X}_3 = \prod_{m=-1}^{\frac{d}{2}-1} X_{(0,2m)} \cdot \prod_{\ell=0}^{k-1} X_{(3\ell+1,d-1)} X_{(3\ell+2,d-1)}. \quad (16)$$

Similarly, we obtain another  $X$ -string cycle by shifting  $\hat{X}_3$  by  $(2, 0)$ :

$$\hat{X}_4 = \prod_{m=-1}^{\frac{d}{2}-1} X_{(2,2m)} \cdot \prod_{\ell=0}^{k-1} X_{(3\ell+3,d-1)} X_{(3\ell+4,d-1)}. \quad (17)$$

All of these operators are shown in Figure 16, up to stabiliser equivalence.

Now, for each  $j \in \{1, 2, 3, 4\}$  consider  $\hat{X}_j$ , change the Pauli terms to  $Z$ s and shift the operator by the vector  $(0, 1)$ . This produces a Pauli- $Z$  operator which we denote by  $\hat{Z}_j$ . Clearly, these Pauli- $Z$  operators commute with all stabilisers. We claim that the operators  $\hat{X}_1, \dots, \hat{X}_4; \hat{Z}_1, \dots, \hat{Z}_4$  are logical operators. Recall that for this the only thing we need to see is whether the anti-commutation matrix  $M = [\epsilon_{i,j}]_{i,j=1}^4$  is invertible in  $\mathbb{F}_2^{4 \times 4}$  where  $\epsilon_{i,j} = 1$  if  $\hat{X}_i$  anti-commutes with  $\hat{Z}_j$ , otherwise  $\epsilon_{i,j} = 0$ , and  $\mathbb{F}_2$  is the two-element field. (Note that sometimes  $M$  is further assumed to be the identity matrix, and one can obtain such logical operators easily by redefining logical  $Z$ -operators as products of the current ones.) From the definition of the operators it is straightforward to calculate that

$$M = \begin{bmatrix} 0 & 0 & 1 & 1 \\ 0 & 0 & 0 & 1 \\ 1 & 0 & 0 & 0 \\ 1 & 1 & 0 & 0 \end{bmatrix}. \quad (18)$$

Since  $M$  is clearly invertible, the proposed operators are indeed logical operators.

The above also proves the upper bound  $\leq d$  on the code distance, i.e. that the minimum weight logical operator has weight at least  $d$ . As we were not able to find logical operators of

lower weight, we conjecture the code distance to be exactly  $d$  for these  $NE^3N$ -codes. Recall that the effective distance of a CSS code with a specified syndrome extraction circuit is the minimum number of total circuit-level failures (according to the considered noise model, i.e. SI-1000 in this case) that causes an undetectable logical failure. One phenomenon that typically results in a reduced effective distance (compared to the code distance) is called “bad hook errors”, see e.g. [41–45]. Hook errors arise from one fault location happening on one ancilla qubit mid-circuit, which then spreads to the data qubits, see [45, Figure 4] for an illustration. In the case of a  $D_1 D_2 \dots D_w$ -directional code, up to stabiliser equivalence, the resulting hook errors are  $\alpha(A_0)_{Q_1} \dots \alpha(A_0)_{Q_\ell}$  and  $\alpha(A_0)_{Q_{w-\ell}} \dots \alpha(A_0)_{Q_w}$  where  $\ell < \frac{w}{2}$ , and they arise from one fault on the ancilla qubit happening just after the  $\ell$ th entangling gate. A hook error is a “bad hook” if the resulting correlated error on the data qubits align with the logical operators, and thus an undetectable logical failure can be a result of less fault locations than the weight of the logical operator. For the  $NE^3N$ -codes, this does not seem to be the case, and checking small examples with Stim’s functionality confirmed it for us. Therefore, we conjecture the effective distance of these codes is exactly  $d$ .

As for (b.1) and (b.2), we can construct the logical operators in a similar way, which we will not detail here.

## A.2 $N^2 E^2 N^2$ -codes encoding six logical qubits

During our investigation, we found two promising families of  $N^2 E^2 N^2$ -codes that encode six logical qubits. The first family, which we presented in Section 3.1, use  $4d^2$  data qubits, admit (conjectured) even distance  $d$ , and are defined on a rectangular torus. We explain below the logical operator structure of these codes. The second family uses approximately half the number of qubits. However, we were unable to find a consistent pattern for the parallelograms of this code family. So the latter family is rather some examples of small CSS code instances that seem to have good QEC performance. Due to the lack of structure, we present the related numerical results in Appendix B.2. From now on, we focus on the first family of  $N^2 E^2 N^2$ -codes.

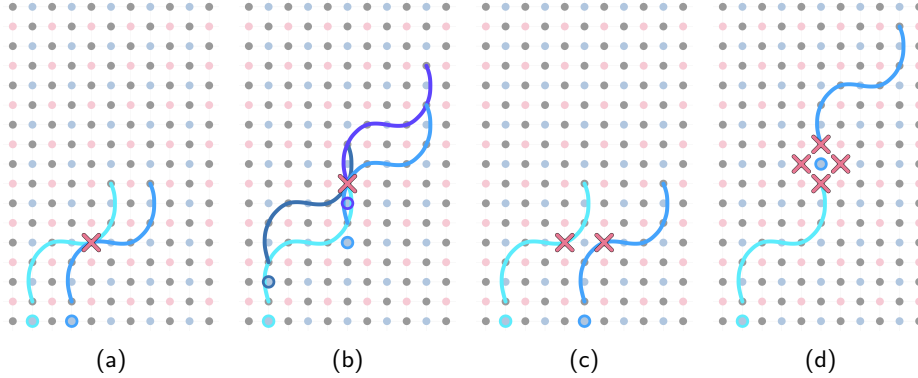


Figure 17: Special type of errors for  $N^2 E^2 N^2$ -codes with “Layout 1”. All are products of  $X$ -errors happening on data qubits just before the first entangling layer of a QEC round. (a) An  $X$ -error on a data qubit that lies in a row of  $Z$ -ancilla qubits, flipping two  $Z$ -stabiliser outcomes. (b) An  $X$ -error on a data qubit that lies in a row of  $X$ -ancilla qubits, flipping four  $Z$ -stabiliser outcomes. (c) A weight-2  $X$ -error on next-nearest neighbour data qubits, also in a row of  $Z$ -ancilla qubits, flipping two  $Z$ -stabilisers. (d) A weight-4  $X$ -error on next-nearest neighbour qubits, flipping two  $Z$ -stabiliser outcomes.

As in Appendix A.1, consider a single  $X$ -error happening on data qubits just before the first entangling layer of syndrome extraction. By referring to Figure 17, we can see

that this error will flip the outcome of either two or four  $Z$ -stabilisers depending on its position. More precisely, if the  $X$ -error occurs in a row of  $Z$ -ancilla qubits, two outcomes are flipped (Figure 17a), otherwise four (Figure 17b). A similar statement can be made for  $Z$ -errors. Hence, the only way a correlated  $XX$ -error flips two  $Z$ -stabiliser outcomes on next-nearest neighbour data qubits is when they lie in a row which contains  $Z$ -ancillas (Figure 17c). However, we point out that there exists a correlated  $XXXX$ -error on next-nearest neighbour data qubits that flips two  $Z$ -stabiliser outcomes (Figure 17d).

During our investigation, we found that the rectangular parallelogram with the following vectors yielded CSS codes with six logical qubits, good performance and relatively low qubit numbers:

$$\vec{v}_1 := (2d, 0), \quad \vec{v}_2 := (0, 4d) \quad (19)$$

where  $d$  is assumed to be an even positive integer.

Now, we examine the logical operator structure of these  $N^2 E^2 N^2$ -codes. Assume that the qubit at  $(0, 0)$  is where a  $Z$ -stabiliser starts (or equivalently, where one of the two middle qubits of an  $X$ -stabiliser is). Due to the structure of the parallelogram, each row of data qubits is a cycle on the torus containing  $d$  data qubits. Hence, based on the structure of the error mechanisms described earlier and shown in Figure 17, we may arrange  $d$   $X$ -errors in a horizontal row with odd  $y$ -coordinate to obtain a Pauli- $X$  operator of weight  $d$  that commutes with all stabilisers, e.g.

$$\hat{X}_1 := \prod_{\ell=0}^{d-1} X_{(2\ell+1,1)}, \quad \hat{X}_2 := \prod_{\ell=0}^{d-1} X_{(2\ell+1,3)}, \quad \hat{X}_3 := \prod_{\ell=0}^{d-1} X_{(2\ell+1,5)}. \quad (20)$$

Notice that we can shift  $\hat{X}_1$  by  $(0, 2)$  and  $(0, 4)$  to obtain  $\hat{X}_2$  and  $\hat{X}_3$ , respectively. We also point out that shifting by  $(0, 6)$  gives an operator that is equivalent up to stabilisers to  $\hat{X}_1 \hat{X}_2 \hat{X}_3$ . Furthermore, shifting by  $(0, 8)$  produces the same operator up to stabiliser equivalence. Indeed, one can see this by taking the product of one row of  $X$ -stabilisers, which is equal to an  $X$ -operator supported on four rows of data qubits that also contain  $Z$ -ancillas.

Next, we consider the diagonal cycles along the vector  $(4, 4)$  starting from a data qubit with even  $x$ - and  $y$ -coordinates. From Figure 17b we see that this provides an  $X$ -Pauli string that commutes with all stabilisers. For instance, we may define the following operators of weight  $d$ :

$$\hat{X}_4 := \prod_{\ell=0}^{d-1} X_{(4\ell,4\ell)}, \quad \hat{X}_5 := \prod_{\ell=0}^{d-1} X_{(4\ell,4\ell+2)}. \quad (21)$$

Again, notice that we can shift  $\hat{X}_4$  by  $(0, 2)$  to get  $\hat{X}_5$ .

Finally, notice that we may combine  $\frac{d}{2} XXXX$ -errors, see Figure 17d, diagonally along the vector  $(4, 8)$  to get a Pauli- $X$  string of weight  $2d$ . For instance, we may define

$$\hat{X}_6 := \prod_{\ell=0}^{\frac{d}{4}-1} \prod_{\vec{d} \in \{\vec{n}, \vec{e}, \vec{w}, \vec{s}\}} X_{(2,1)+\ell(4,8)+\vec{d}}. \quad (22)$$

All the operators from Equations (20) to (22) are depicted in Figure 18.

Now, for each  $j \in \{1, \dots, 6\}$  consider  $\hat{X}_j$ , change the Pauli terms to  $Z$ 's and shift the operator by the vector  $(1, 1)$ . This produces a Pauli- $Z$  operator which we denote by  $\hat{Z}_j$ . Clearly, these Pauli- $Z$  operators commute with all stabilisers. In order to see that the

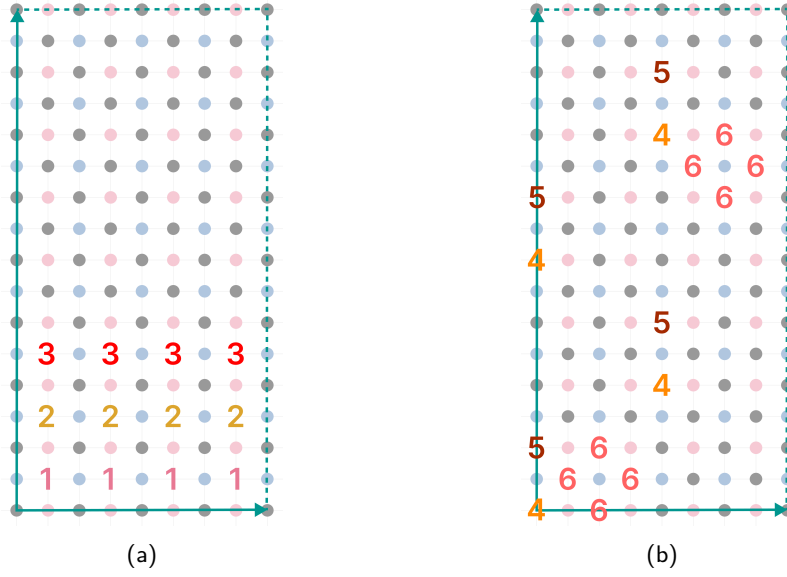


Figure 18:  $X$ -logical operators  $\hat{X}_1, \dots, \hat{X}_6$  for the  $N^2E^2N^2$ -code on the rectangle specified in Equation (19) for  $d = 4$ . They are depicted as strings of numbers corresponding to their indices specified in the text, each coloured differently. The  $Z$ -logical operators can be obtained by translating their  $X$  counterparts by  $(1, 1)$  and changing the Pauli terms to  $Z$ s.

operators  $\hat{X}_1, \dots, \hat{X}_6; \hat{Z}_1, \dots, \hat{Z}_6$  are logical operators, we calculate the anti-commutation matrix:

$$M = \begin{bmatrix} 0 & 0 & 0 & 1 & 0 & 1 \\ 0 & 0 & 0 & 0 & 1 & 1 \\ 0 & 0 & 0 & 1 & 0 & 0 \\ 0 & 1 & 0 & 0 & 0 & 0 \\ 1 & 0 & 1 & 0 & 0 & 0 \\ 1 & 0 & 0 & * & * & 0 \end{bmatrix}. \quad (23)$$

Note that we left two elements unspecified, denoted by asterisks, which may be 0 or 1 depending on the value of  $d$ . Notice that these values do not impact the invertibility of  $M$ , since the top-left  $3 \times 3$  block only contains 0 elements and the top-right and bottom-left  $3 \times 3$  blocks are both invertible, making  $M$  invertible. Therefore, the proposed operators are indeed logical operators.

The above also proves the upper bound  $\leq d$  on the code distance, and since we were not able to find logical operators of smaller weights, we conjecture the code distance to be exactly  $d$ . As for the effective distance, since it does not seem like there are any bad hooks for these  $N^2E^2N^2$ -codes, and checking small examples with Stim's functionality confirmed that, we conjecture the effective distance to be  $d$ .

### A.3 $N^2E^3N^2$ -codes encoding twelve logical qubits

Now, consider the  $N^2E^3N^2$ -codes on parallelogram  $\mathcal{P}(\vec{v}_1, \vec{v}_2)$ , with its stabilisers laid out according to "Layout 1", as in the previous two subsections. We found three families of  $N^2E^3N^2$ -codes that encode twelve logical qubits and perform well. The first two of these are defined as follows:

- (1)  $\vec{v}_1 = (3d, 0)$ ,  $\vec{v}_2 = (3d - 6, 4d - 8)$  for  $d \in \{4, 6, 8, \dots\}$ , giving a  $[[6d^2 - 12d, 12, \leq d]]$  CSS code.



(2)  $\vec{v}_1 = (3d, 0)$ ,  $\vec{v}_2 = (0, 4d)$  for  $d \in \{2, 4, 6, 8, \dots\}$ , giving a  $[[6d^2, 12, \leq d]]$  CSS code.

Note again that the distance is given as an upper estimation. In Section 3 we presented results for family (1), because they use  $O(d)$  fewer physical qubits for a given conjectured distance  $d$  compared to family (2). However, family (2) is defined on a rectangle  $\mathcal{P}$ , therefore it may be a more natural choice. The three codes from family (2) with  $d = 4, 6, 8$  that we obtained numerical results for are shown in Table 3 and Figure 23. As mentioned above, we also found a third family of  $N^2 E^3 N^2$ -codes that use fewer qubits than (1)–(2), but for which we were unable to find a clear unifying pattern. They are also included in Table 3 and plotted in Figure 24.

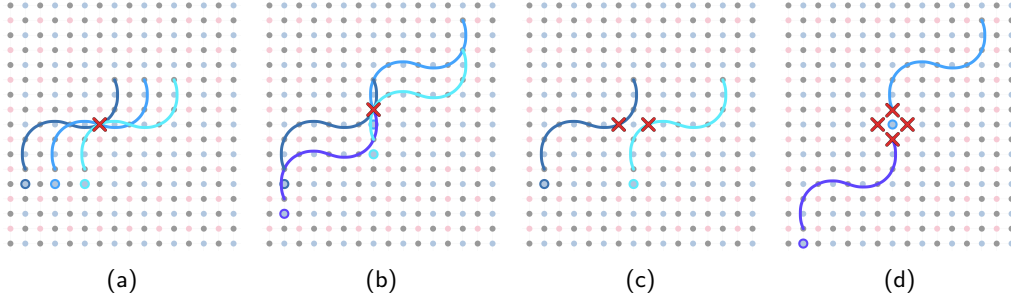


Figure 19: Special type of errors for  $N^2 E^3 N^2$ -codes with “Layout 1”. All are products of  $X$ -errors taking place on data qubits just before the first entangling layer of a QEC round. (a) An  $X$ -error on a data qubit which lies in a row of  $Z$ -ancilla qubits and flips three measurement outcomes. (b) An  $X$ -error on a data qubit which lies in a row of  $X$ -ancilla qubits and flips four measurement outcomes. (c) A weight-2  $X$ -error on two next-nearest neighbour data qubits which lie on the same  $Z$ -ancilla qubit row, and flip two measurement outcomes. (d) A weight-4  $X$ -error on four nearest-neighbour data qubits of a  $Z$ -ancilla qubit, flipping two measurement outcomes.

Next, we describe special types of errors that will be the building blocks of constructing the logical operators. Consider an  $X$ -error occurring on a data qubit right before the first entangling layer of a QEC round. If this data qubit lies on a row of  $Z$ -ancilla qubits, then it will flip three measurement outcomes (see Figure 19a), otherwise, it will flip four (see Figure 19b). Combining two  $X$ -errors on next-nearest neighbour data qubits that both lie in a row of  $Z$ -ancilla qubits gives an  $XX$ -error which flips just two measurement outcomes (see Figure 19c). Finally, the  $XXXX$ -error supported on the four nearest-neighbours of a  $Z$  ancilla qubit flips only two measurement outcomes, as can be seen in Figure 19d.

From here we aim to describe the logical operator structure of code family (1), and note that they can be similarly described for family (2) as well. Assume that the data qubit at  $(0, 0)$  is where a  $Z$ -stabiliser starts (or equivalently, where the three middle qubits of an  $X$ -stabiliser is). Due to the structure of the parallelogram, each row of data qubits is a cycle on the torus containing  $\frac{3}{2}d$  data qubits. Based on Figure 19c, we can define an operator of weight  $d$  that commutes with all the stabilisers as:

$$\hat{X}_1 := \prod_{\ell=0}^{\frac{d}{2}-1} X_{(6\ell+1,1)} X_{(6\ell+3,1)}. \quad (24)$$

We also define five other operators by shifting  $\hat{X}_1$ . More precisely, define  $\hat{X}_{i+2j}$  ( $i \in \{1, 2\}$ ,  $j \in \{0, 1, 2\}$ ) to be the operator we obtain by shifting  $\hat{X}_1$  with the vector  $(2j + 2i - 2, 2j)$ .

Next, notice that we may combine  $\frac{d}{2} - 1$  many  $XXXX$ -errors, see Figure 17d, diagonally along the vector  $(6, 8)$  to obtain a Pauli- $X$  operator of weight  $2d - 4$  that commutes

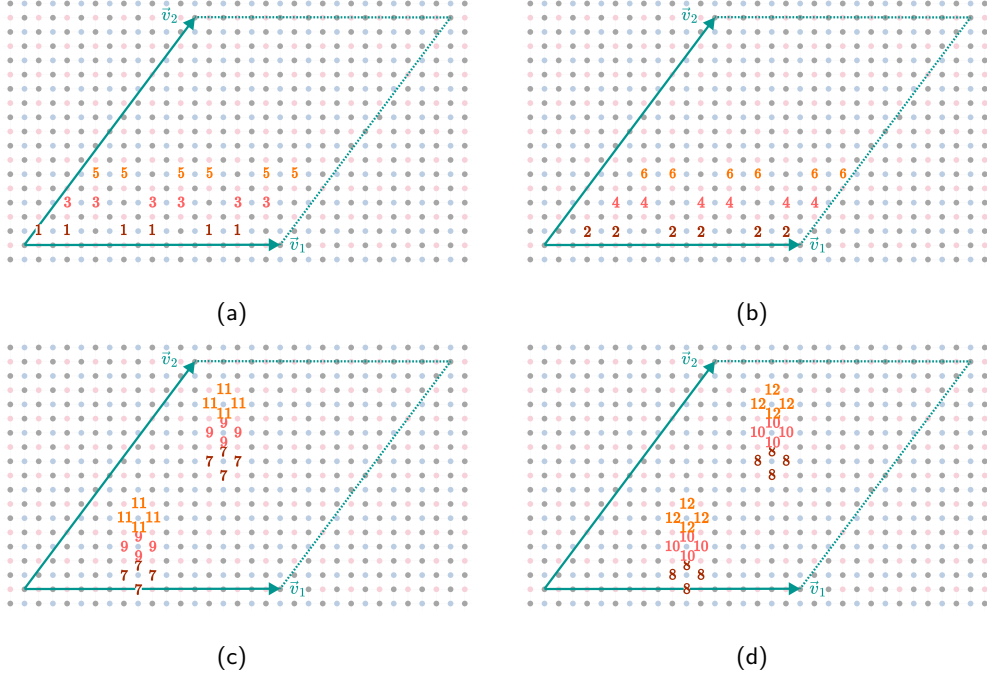


Figure 20:  $X$ -logical operators for the  $d = 6$  code from family (1), where  $\vec{v}_1 = (18, 0)$  and  $\vec{v}_2 = (12, 16)$ . The logical operator  $\hat{X}_k$  consists of the product of  $X$ s on each data qubit marked with the integer  $k$ . For clarity, the twelve operators are distributed over four panels. Specifically, (a) contains  $\hat{X}_1, \hat{X}_3, \hat{X}_5$ , (b)  $\hat{X}_2, \hat{X}_4, \hat{X}_6$ , (c)  $\hat{X}_7, \hat{X}_9, \hat{X}_{11}$  and (d)  $\hat{X}_8, \hat{X}_{10}, \hat{X}_{12}$ .

with all stabilisers, for instance, we may define:

$$\hat{X}_7 := \prod_{\ell=0}^{\frac{d}{2}-2} \prod_{\vec{d} \in \{\vec{n}, \vec{e}, \vec{w}, \vec{s}\}} X_{(8,1)+\vec{d}+\ell(6,8)} \quad (25)$$

Similarly as before, we define five more Pauli- $X$  operators: let  $\hat{X}_{7+i+2j}$  ( $i \in \{0, 1\}, j \in \{0, 1, 2\}$ ) be the operator we obtain by shifting  $\hat{X}_7$  with the vector  $(2i, 2j)$ .

Overall we defined twelve Pauli- $X$  operators  $\hat{X}_1, \dots, \hat{X}_{12}$  which we claim to be the  $X$ -logical operators, see Figure 20 for an illustration of the distance 6 case. For each  $j \in \{1, \dots, 12\}$  consider  $\hat{X}_j$ , change its Pauli terms to  $Z$ s and shift the operator by the vector  $(1, 1)$ . This defines a Pauli- $Z$  operator which we denote by  $\hat{Z}_j$ . Now, we compute the anti-commutation matrix:

$$M = \begin{bmatrix} 0 & 0 & 0 & 0 & 0 & 0 & 1 & 0 & 0 & 0 & 0 & 0 \\ 0 & 0 & 0 & 0 & 0 & 0 & 1 & 1 & 0 & 0 & 0 & 0 \\ 0 & 0 & 0 & 0 & 0 & 0 & 1 & 1 & 1 & 1 & 0 & 0 \\ 0 & 0 & 0 & 0 & 0 & 0 & 0 & 1 & 0 & 1 & 0 & 0 \\ 0 & 0 & 0 & 0 & 0 & 0 & 0 & 0 & 0 & 1 & 0 & 1 \\ 0 & 0 & 0 & 0 & 0 & 0 & 0 & 0 & 1 & 0 & 1 & 0 \\ 1 & 0 & 0 & 0 & 0 & 0 & 0 & 0 & 0 & 0 & 0 & 0 \\ 1 & 1 & 0 & 0 & 0 & 0 & 0 & 0 & 0 & 0 & 0 & 0 \\ 1 & 0 & 0 & 1 & 0 & 0 & 0 & 0 & 0 & 0 & 0 & 0 \\ 1 & 1 & 1 & 0 & 0 & 0 & 0 & 0 & 0 & 0 & 0 & 0 \\ 0 & 0 & 0 & 1 & 1 & 1 & 0 & 0 & 0 & 0 & 0 & 0 \\ 0 & 0 & 1 & 0 & 0 & 1 & 0 & 0 & 0 & 0 & 0 & 0 \end{bmatrix}. \quad (26)$$

It is straightforward to see that this matrix is invertible, which means that the proposed operators are indeed logical operators. This also proves the upper bound  $\leq d$  on the code distance. Since we were not able to find logical operators of smaller weights, we conjecture the code distance to be exactly  $d$ . As for the effective distance, it does not seem like there are any bad hooks for these  $N^2E^3N^2$ -codes, and checking small examples with Stim’s functionality confirmed this. Hence, we conjecture the effective distance to be also  $d$ .

## B Simulation details and additional results

In this section, we provide further details on the simulation methodology and additional results for some directional codes not presented in Section 3, except in Figures 10, 12 and 14. The  $NE^3N$ -codes presented here perform slightly worse than those in Section 3, but use slightly less physical qubits. Contrastingly, the  $N^2E^2N^2$ -codes perform as well as those in Section 3 and do so using almost half as many qubits, but we could not determine a consistent pattern for them that can be extended to arbitrary distance. Finally, of the two families of  $N^2E^3N^2$ -codes presented here, one family matches the performance of those in Section 3 but with increased qubit number, while the other, similar to the  $N^2E^2N^2$ -codes in this section, match the performance with reduced qubit count, but do not belong to an obvious pattern. Overall, these additional codes provide interesting alternatives to those in Section 3 in their own right, and may even be better choices in certain scenarios - e.g, particularly small hardware. All of these additional codes’ circuits, as well as their parity check matrices, can be found in [51].

### B.1 Simulation details

In this subsection, we provide further details on our simulation methodology. We used “stim” [58] to sample our noisy circuits and BP-OSD [46–48, 59] to decode the samples for all circuits. For each data point, we sampled until the error bars were acceptably small. For most points, this meant  $10^5$  shots, going up to  $3 \times 10^6$  for the lower  $p$ ’s. The sampling and decoding were handled by the “sinter” decoding sampler, which efficiently distributes the tasks across multiple CPU cores.

Across all the experiments, the BP-OSD parameters used were set to 15 for both the number of BP iterations and the OSD order. We found this gave an acceptable balance between accuracy and speed. We note that there are decoders that significantly speed up the OSD part of the decoder, [60, 61], however they were not available at the time this research was performed. There are also recently proposed alternative hypergraph decoders that improve on the runtime and/or accuracy of BP-OSD, but were unavailable to use at the time, see e.g. [55, 62, 63]. All of our simulations, including the initial explorations and parallelogram searches, used a total of  $\approx 46$  CPU-core-years.

For each experiment with directional codes, we constructed the circuit in terms of the following gates:  $Z$ -basis reset (R),  $Z$ -basis measurement (M), the iSWAP entangling gate, the Hadamard gate (H), the phase gate (S) and the  $\frac{\pi}{2}$ - $X$ -rotation ( $\sqrt{X}$ ). These circuits all can be executed under degree-4 (Figure 1a) and some of them even under degree-3 connectivity (Figure 1b), see Table 1.

As for the BB codes and RPC circuits, we used the same gates, except instead of iSWAP we used the controlled-phase gate (CZ). The RPC circuits are constructed in the standard way, i.e. under square-grid connectivity. We note that circuits for the RPC can also be constructed on a hexagonal-grid with CZ gates, and with iSWAP gates both on square- and hex-grid. These alternative circuits have similar QEC performance, see [31].

Note that the BB codes require a degree-6 connectivity device that can be obtained from considering a toric square-grid and adding two long-range connections to each qubit. For the particular BB codes we consider here, e.g. the gross code, these long-range connections are between pairs of qubits that are Manhattan-distance 9 apart from each other (6 in the horizontal/vertical and 3 in the perpendicular direction), see [28, Figure 1B]. However, again note that the noise model we use (SI-1000) does not take these long-range connections and the increased connectivity into account, as mentioned in Section 3.

## B.2 Additional results

Directions	$\llbracket n, k, \leq d \rrbracket$	$\vec{v}_1$	$\vec{v}_2$	Net encoding rate
$NE^3N$	$\llbracket 24, 4, 4 \rrbracket$	(12, 0)	(6, 4)	$\frac{1}{12}$
$NE^3N$	$\llbracket 120, 4, 8 \rrbracket$	(24, 0)	(12, 8)	$\frac{1}{60}$
$N^2E^2N^2$	$\llbracket 32, 6, 3 \rrbracket$	(-2, 8)	(6, 8)	$\frac{1}{11}$
$N^2E^2N^2$	$\llbracket 72, 6, 5 \rrbracket$	(-4, 8)	(14, 8)	$\frac{1}{24}$
$N^2E^2N^2$	$\llbracket 128, 6, 7 \rrbracket$	(-12, 8)	(8, 16)	$\frac{1}{42}$
$N^2E^2N^2$	$\llbracket 200, 6, 9 \rrbracket$	(-10, 16)	(20, 8)	$\frac{1}{67}$
$N^2E^3N^2$	$\llbracket 96, 12, 4 \rrbracket$	(12, 0)	(0, 16)	$\frac{1}{16}$
$N^2E^3N^2$	$\llbracket 216, 12, 6 \rrbracket$	(18, 0)	(0, 24)	$\frac{1}{36}$
$N^2E^3N^2$	$\llbracket 384, 12, 8 \rrbracket$	(24, 0)	(0, 32)	$\frac{1}{64}$
$N^2E^3N^2$	$\llbracket 96, 12, 6 \rrbracket$	(18, 8)	(-6, 8)	$\frac{1}{16}$
$N^2E^3N^2$	$\llbracket 144, 12, 8 \rrbracket$	(-12, 8)	(24, 8)	$\frac{1}{24}$
$N^2E^3N^2$	$\llbracket 240, 12, 10 \rrbracket$	(0, 16)	(-30, 8)	$\frac{1}{40}$

Table 3: The directional codes presented in this section, alongside their parameters and net encoding rate rounded to the nearest integer like in [28].

As mentioned in Section 3, we discovered additional directional codes with noteworthy characteristics, but that we chose not to present in Section 3 outside of Figures 10, 12 and 14, so we present the remaining codes here. In Table 3 we list these additional directional codes, alongside their parameters and net encoding rate.

In Figure 21 we show a comparison of (b.1) and (b.2)  $NE^3N$ -codes. We see that while the (b.1) codes perform slightly worse, they do so with a reduced qubit number. Hence, we anticipate that these smaller (b.1)  $NE^3N$ -codes offer attractive options for a first attempt at an experimental realisation of our codes.

In Figure 22 we present additional  $N^2E^2N^2$ -codes, which are of (conjectured) odd-distance. We verified the effective distance for the  $\llbracket 32, 6, 3 \rrbracket$ -code numerically using Stim.

Figure 23 shows family (2) (as described in Appendix A.3) of the  $N^2E^3N^2$ -codes that perform well but with slightly increased qubit number compared to those in Figure 13. Finally, Figure 24, shows a family of  $N^2E^3N^2$ -codes that do not have a consistent pattern through which arbitrarily large codes can be constructed. Nevertheless, they use fewer qubits than both families shown in Figures 13 and 23 while also having lower logical error probability.

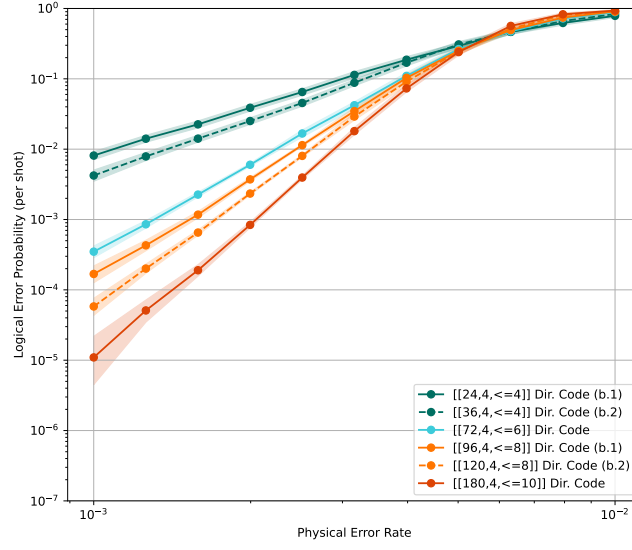
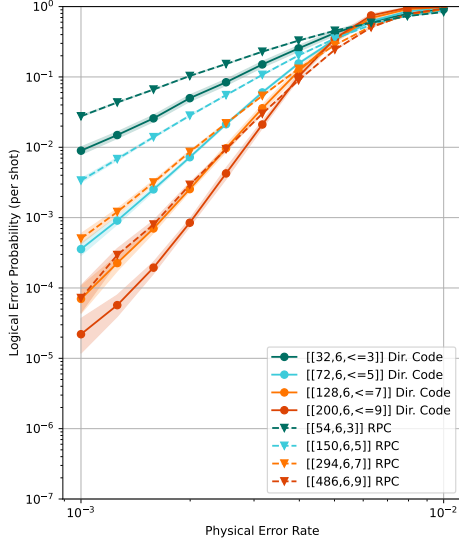
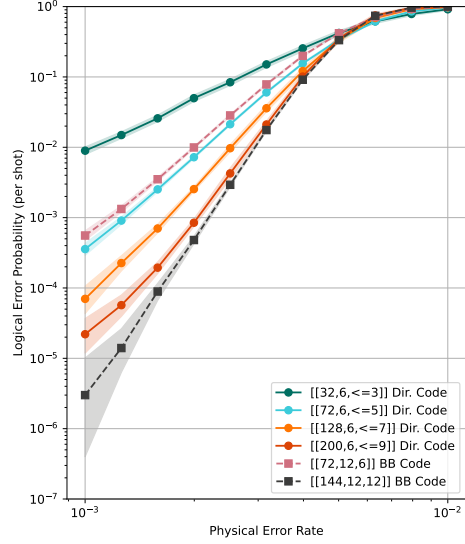


Figure 21:  $NE^3N$ -codes of case (b.1) vs (b.2). Shown as solid lines are simulations for cases (b.1) and (a), which perform slightly worse but with reduced physical qubit count, and the case (b.2) codes as dashed lines. Recall that cases (b.1) and (b.2) only apply where  $4 \mid d$ .



(a)



(b)

Figure 22: Comparison of  $N^2E^2N^2$ -codes (odd distance) to (a) RPCs and (b) BB codes under SI-1000 circuit-level Pauli noise.

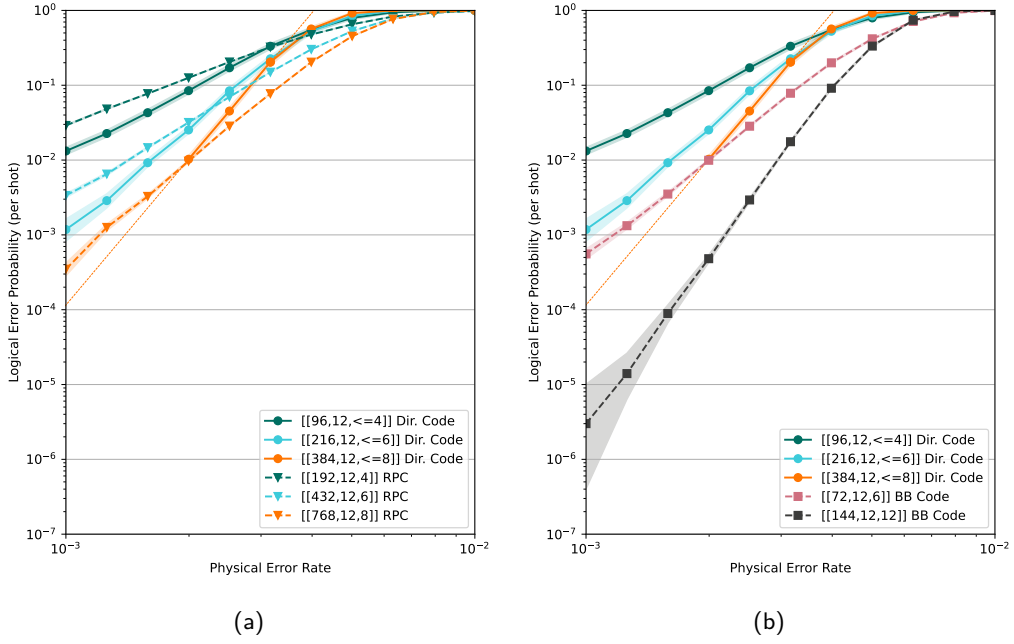


Figure 23:  $N^2 E^3 N^2$ -codes with parameters  $[[6d^2, 12, d]]$ . Comparison of these codes to (a) RPCs and (b) BB codes are shown. Due to the size of the  $[[384, 12, \leq 8]]$  code, we stopped simulations at  $p = 10^{-2.7}$ , and instead provide a line fit for the remaining points.

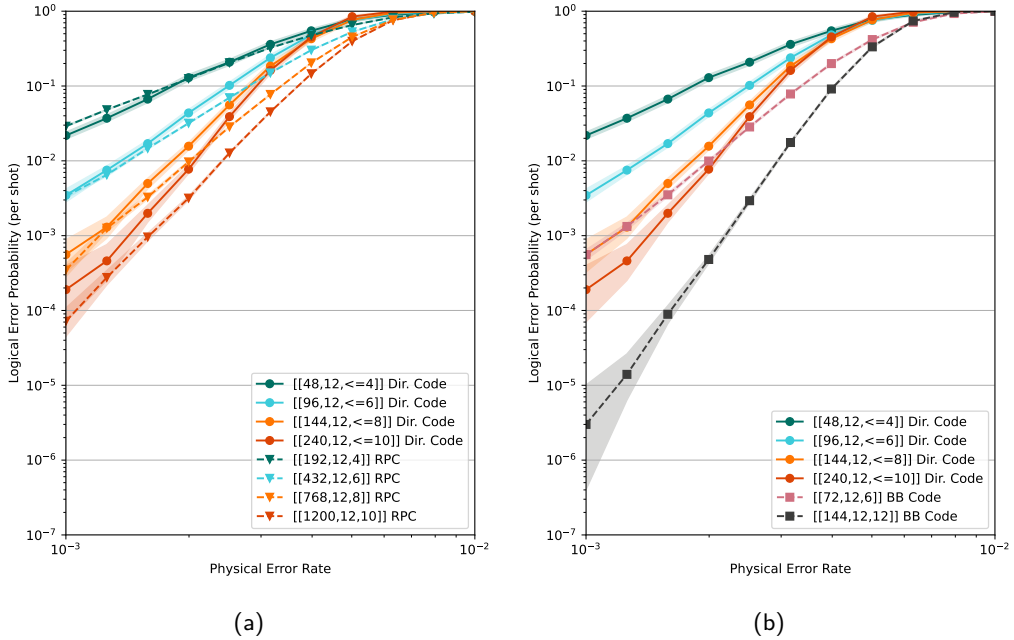


Figure 24:  $N^2 E^3 N^2$ -codes that do not follow a regular pattern, instead found experimentally. Comparison of these codes to (a) RPCs and (b) BB codes are shown. Note that the  $[[48, 12, \leq 4]]$  code is the same as the code presented in Section 3.3.